https://doi.org/10.5194/egusphere-2023-155
Preprint. Discussion started: 3 February 2023

Radiative effect by cirrus cloud and contrails – A comprehensive sensitivity study

Kevin Wolf[1], Nicolas Bellouin[1,2], and Olivier Boucher[1]

[1]Institut Pierre-Simon Laplace, Sorbonne Université / CNRS, Paris, France
[2]Department of Meteorology, University of Reading, Reading, United Kingdom

Correspondence: Kevin Wolf (kevin.wolf@ipsl.fr)

Abstract. Natural cirrus clouds and contrails cover about 30% of the Earth's mid-latitudes and up to 70% of its Tropics. Due to their widespread occurrence, cirrus have a considerable impact on the Earth energy budget, which, on average, leads to a warming net radiative effect (solar + thermal-infrared). However, whether the instantaneous radiative effect (RE) of natural cirrus or contrails is positive or negative depends on their microphysical, macrophysical, and optical, as well as radiative properties of the environment. This is further complicated by the fact that the actual ice crystal shape is often unknown and thus ice clouds remain one of the components that are least understood in the Earth's radiative budget.

The present study aims to separate the effect on cirrus RE of eight parameters: solar zenith angle, ice water content, ice crystal effective radius, cirrus temperature, surface albedo, surface temperature, liquid water cloud optical thickness of an underlying cloud, and three ice crystal shapes. In total, 94,500 radiative transfer simulations have been performed, spanning the parameter ranges that are typically associated with natural cirrus and contrails. The multi-dimensionality and complexity of the 8-dimension parameter space makes it impractical to discuss all potential configurations in detail. Therefore, specific cases are selected and discussed.

The ice crystal effective radius has the largest impact on solar, thermal-infrared (TIR), and net RE. The second most important parameter is the ice water content, which impacts the solar and terrestrial RE equally. Solar and TIR RE have opposite signs, meaning that the ice water content has a relatively small impact on net RE. Beyond the ice crystal effective radius and the ice water content, the solar RE of cirrus is determined by solar zenith angle, surface albedo, liquid cloud optical thickness, and the ice crystal shape in descending priority. RE in the TIR spectrum is dominated by the surface temperature, the ice cloud temperature, the liquid water cloud optical thickness, and the ice crystal shape. Net RE is controlled by the surface albedo, the solar zenith angle, and the surface albedo in decreasing importance. The relative importance of the studied parameters differs depending on the ambient conditions and during nighttime the net RE is equal to the TIR RE.

The data set generated in this work is publicly available. It can be used to compute the radiative effect of cirrus clouds, contrails, and contrail cirrus instead of full radiative transfer calculations.

1 Introduction

Cirrus clouds cover large areas of the Earth, with cloud cover estimates of 30 % in the mid-latitudes and up to 70 % in the tropics (Liou, 1986; Wylie and Menzel, 1999; Chen et al., 2000; Sassen et al., 2008; Nazaryan et al., 2008). Due to their widespread occurrence, cirrus can have a considerable impact on the global energy budget. In addition to cirrus, air traffic leads to the formation of condensation trails, also termed contrails, which are optically and geometrically thin clouds with similar radiative effects as thin natural cirrus (Liou, 1986). For the sake of simplicity, the term cirrus is used interchangeably for natural cirrus, contrail-induced cirrus, and contrails throughout this article.

Depending on ambient conditions, contrails are short lived ($t < 10$ min) but can persist up to a day when the surrounding air mass is sufficiently cold and moist (Jensen et al., 1994; Schumann, 1996; Haywood et al., 2009). In such conditions, persistent contrails transition from line-shaped clouds to larger cloud fields (Unterstrasser and Stephan, 2020). Modeling and satellite studies have estimated that contrail and contrail-induced cirrus cloud cover can reach up to 6 to 10 % over Europe (Burkhardt and Kärcher, 2011; Quaas et al., 2021).

Under most circumstances cirrus have a cooling effect in the solar wavelength range (0.2–3.5 μm, sometimes called shortwave) and a heating effect in the thermal-infrared (TIR) wavelength range (3.5–100 μm, sometimes also termed longwave or terrestrial). The net radiative effect (solar cooling + TIR warming) is often a warming as the TIR effect dominates (Chen et al., 2000). By combining satellite observations and radiative transfers (RT) simulations, Chen et al. (2000) estimated a global annual mean cirrus cloud radiative effect (RE) of $-25.3\ \mathrm{W\,m^{-2}}$ in the solar wavelength range and $30.7\ \mathrm{W\,m^{-2}}$ in the TIR wavelength range, leading to a positive net effect of $5.4\ \mathrm{W\,m^{-2}}$. However, whether the instantaneous RE of natural cirrus or contrails is positive or negative depends on their microphysical, macrophysical, and optical, as well as radiative properties of the environment. The cloud properties relevant to the RE of the cloud are primarily cloud altitude, cloud temperature, ice water content, ice crystal shape (also called crystal habit), and the orientation of the ice crystals (Fu and Liou, 1993; Stephens et al., 2004; Campbell et al., 2016). Furthermore, the underlying surface properties, i.e., surface albedo and surface temperature, as well as gaseous absorption and additional underlying cloud layers, also have an effect on the cirrus RE. Dynamical processes in the atmosphere have a strong influence on those parameters, for example lifting of air masses along warm conveyor belts or cloud anvils, that lead to a variety of ice crystal shapes and crystal surface roughness (Freudenthaler et al., 1996; Wendisch et al., 2007; Yang et al., 2010; Krämer et al., 2016; Luebke et al., 2016). As a result, the actual distribution of crystal shapes within a cirrus and the related RE are often unclear. Thus ice clouds remain one of the components that are least understood in the Earth's radiative budget (Stevens and Bony, 2013; Bauer et al., 2015; Bickel et al., 2020) and this lack of understanding contributes to uncertainties in the climate impact of aviation (Lee et al., 2021).

To estimate the radiative impact of a cloud as well as related potential uncertainties and sensitivities, RT simulations represent a helpful tool despite their complexity as in the case of ice clouds. While the atmospheric RT in liquid water clouds composed of spherical cloud droplets can rely on geometric optics or Mie-scattering theory (Mie, 1908; van de Hulst, 1981), RT simulations in ice clouds are made complicated by the non-spherical shape of ice crystals. The way non-spherical crystals interact with radiation, i.e., through their single-scattering phase function, has to be determined by computationally-expensive methods, like

https://doi.org/10.5194/egusphere-2023-155
Preprint. Discussion started: 3 February 2023

ray tracing (Bi et al., 2014), Monte Carlo simulations (Macke et al., 1996b, a), or the T-matrix method (Mishchenko, 2020). Due to the computational burden of such accurate simulations, approximations, i.e., ice crystal parameterizations of radiative properties, are often developed and validated against the more precise calculations (Takano and Liou, 1989; Fu, 1996; Yang et al., 2000, 2013). More recent ice crystal parameterizations by Yang et al. (2000), Baum et al. (2005), Baum et al. (2007), and Yang et al. (2013) in combination with the latest RT models allow to determine the radiative impact of cirrus clouds with acceptable computational cost and accuracy. By varying the microphysical and macrophysical properties of the cirrus, as well as the surface properties in the RT model, the natural range of cirrus and their environment can be represented and the RE can be estimated. Furthermore, uncertainties due to the insufficiently known crystal shape can be assessed.

Multiple studies that aimed to investigate the impact of a certain parameter, like the crystal size distribution, on the cloud RE have been performed in the past. Fu and Liou (1993) as well as Yang et al. (2010) focused on the effects of the selected ice crystal habit and the ice water path. The effect of the ice crystal size was analyzed by Zhang et al. (1999), while Mitchell et al. (2011) looked into the implications of the crystal size distribution. A comprehensive study of cirrus radiative effects was conducted by Schumann (2012), who aimed to derive an approximate model to estimate the cloud RE. While those studies are valuable, none of them presents a comprehensive sensitivity study across all relevant cloud and environmental input parameters.

Therefore, we present a study that separates the effect of eight selected parameters on the cirrus RE. This article is intended as a parametric sensitivity study and aims to compare the effects of different input parameters with different units and value ranges. We sample the input parameter range, restricted to values that are typically associated with ice clouds, to identify the relative importance of the different input parameters. Furthermore, we aim to provide an open-access data set, which allows the user to extract cloud REs for user-specific combinations of the input parameters.

The study is structured in the following way. Section 2 introduces the selected parameter space, the RT model, and outlines basic definitions as well as methods used in the paper. Subsequently, Section 3 presents the results from the RT simulations.

2 Methods and Definitions

2.1 Concept of radiative effect and albedo

The radiative impact of any perturbation, e.g., clouds, is quantified by the concept of the radiative effect (RE). The RE is defined as the net difference in downward and upward irradiance ($F^{\downarrow} - F^{\uparrow}$) between the perturbed and unperturbed condition. In the case of clouds, the cloud radiative effect (CRE, denoted here as ΔF) is the difference in fluxes between the cirrus (F_{c}) and cirrus-free (F_{cf}) atmosphere at a given altitude z (Ramanathan et al., 1989; Stapf et al., 2021; Luebke et al., 2022):

$$\begin{aligned}\Delta F(z) = F_{\mathrm{c}}(z) - F_{\mathrm{cf}}(z) = {} & \left[F^{\downarrow}(z) - F^{\uparrow}(z)\right]_{\mathrm{c}} \\ & - \left[F^{\downarrow}(z) - F^{\uparrow}(z)\right]_{\mathrm{cf}}, \end{aligned} \tag{1}$$

where the upward and downward irradiances are both counted positive. The net RE can be split into a solar:

$$\Delta F_{\mathrm{sol}}(z) = \left[F^{\downarrow}_{\mathrm{sol}}(z) - F^{\uparrow}_{\mathrm{sol}}(z)\right]_{\mathrm{c}} - \left[F^{\downarrow}_{\mathrm{sol}}(z) - F^{\uparrow}_{\mathrm{sol}}(z)\right]_{\mathrm{cf}} \tag{2}$$

https://doi.org/10.5194/egusphere-2023-155
Preprint. Discussion started: 3 February 2023

and a thermal-infrared component:

$$\Delta F_{\mathrm{tir}}(z) = \left[F_{\mathrm{tir}}^{\downarrow}(z) - F_{\mathrm{tir}}^{\uparrow}(z)\right]_{\mathrm{c}} - \left[F_{\mathrm{tir}}^{\downarrow}(z) - F_{\mathrm{tir}}^{\uparrow}(z)\right]_{\mathrm{cf}}. \tag{3}$$

Within this study, the CRE is calculated for the top of atmosphere (TOA) at 15 km if not stated otherwise.

In addition to the RE, the albedo α describes the interaction of a cloud or a surface with the incident radiation. The scene albedo $\alpha(\lambda)$ is defined as the ratio of the reflected, upward irradiance $F^{\uparrow}$ in relation to the incident, downward irradiance $F^{\downarrow}$ and is given by:

$$\alpha(\lambda) = \frac{F^{\uparrow}(\lambda)}{F^{\downarrow}(\lambda)}. \tag{4}$$

The scene albedo depends on the surface albedo that varies spectrally. Nevertheless, the spectral variation of the surface albedo is kept constant in this study. In the TIR wavelength range α_{srf} is assumed to be 0, which leads to an emissivity $\epsilon = 1$ with the Earth's surface thus acting as a blackbody (Wilber, 1999).

2.2 Radiative transfer simulation set-up

Upward and downward irradiances $F^{\uparrow}$ / $F^{\downarrow}$ were simulated with the library for Radiative transfer (libRadtran, Emde et al., 2016). The solar irradiances F_{sol} cover a wavelength range from 0.3 to 3.5 μm, which represents 97.7 % of the total incoming solar radiation (0–10 μm). The TIR irradiances include wavelengths from 3.5 to 75 μm, representing 99.3 % of the integrated blackbody radiation (3.5 to 100 μm) at 285 K (12°C). libRadtran was run as a one-dimensional (1D) RT solver in which clouds are uniform on the horizontal and lateral photon transport between columns is not considered. This approximation is called independent pixel approximation (IPA, Stephens et al., 1991; Cahalan et al., 1994). We regard 1D simulations as appropriate as we focus on the basic dependencies of ΔF on the driving parameters. We also restrain the simulations to fully cloud covered scenes. Irradiances are therefore calculated with the Discrete Ordinate Radiative Transfer model (DISORT) 2.0 solver by Stamnes et al. (2000). The required number of streams was iteratively determined and set to 16 streams, which provides sufficient accuracy while limiting computational time. The trade-off between accuracy and computational time is detailed in Appendix B. The spectral TOA solar irradiance is provided by Kurucz (1992). The RT simulations consider molecular absorption using the medium resolution REPTRAN parameterization from Gasteiger et al. (2014).

The sensitivity of solar, TIR, and net cloud RE ΔF is estimated by varying eight parameters. The parameter ranges were chosen to represent commonly observed cirrus, contrail cirrus properties, and environment parameters.

- The daily course of the Sun position is represented by solar zenith angles θ ranging from 0° and 70°. Larger θ values are omitted to avoid numerical instability that would require more streams in the calculation.
- The Earth's surface albedo, α_{srf} ranges from 0 to 1, which represents the full possible range. Therefore, the α_{srf} in the solar wavelength range is varied from 0 to 1 to include surface conditions ranging from open ocean over marginal sea ice zones to domains with full sea ice or snow cover. (Baldridge et al., 2009; Gardner and Sharp, 2010; Meerdink et al., 2019; Gueymard et al., 2019).

Table 1. Cirrus temperature and pressure level at 223, 233, and 243 K depending on the surface temperature and associated atmosphere profile.

Cirrus temperature	US Standard (`afglus`)	Tropical (`afglt`)	Subarctic winter (`afglsw`)
223 K (-50°C)	10.0 km | 260 hPa	12.1 km | 210 hPa	7.6 km | 350 hPa
233 K (-40°C)	8.5 km | 333 hPa	10.6 km | 263 hPa	6.2 km | 437 hPa
243 K (-30°C)	7.0 km | 414 hPa	9.0 km | 325 hPa	4.7 km | 540 hPa

- The surface temperature T_{srf} is set to -40°C, 0°C, and 40°C representing Arctic, mid-latitude, and tropical or desert conditions, respectively. The atmospheric profiles are selected depending on T_{srf} using the subarctic winter (`afglsw`, T_{srf} = 273 K), tropical (`afglt`, T_{srf} = 313 K), or the US standard (`afglus`, elsewhere) profiles after Anderson et al. (1986). Directly related to different temperature profiles is a variation in the relative humidity profile, which primarily impacts the RT in the TIR wavelength range but also, to a minor extent, in the solar wavelength range by water vapor absorption. This effect is not separated from the temperature variation. The altitude of the cirrus cloud base depends on the selected atmosphere profile (T_{srf}) and the selected cirrus temperatures T_{ice}. T_{ice} are selected to span the temperature range in which contrails and cirrus typically form (Krämer et al., 2020). The resulting cirrus cloud base is set to the altitude where the temperature of the profile equals the desired T_{ice}. The cloud geometric thickness Δz is not varied in this study and set to 0.2 km. Cirrus temperatures and related cirrus base altitudes are listed in Table 1.

- Three different ice crystal shapes are considered in this study. The tables after Yang et al. (2000) are selected among the available set of ice optics parameterizations in libRadtran. 'Rough-aggregates' were chosen as the primary ice crystal habit. The ice parameterization is assumed to represent complex-shaped, non-spherical ice crystals that can be found in aged contrails and cirrus. In addition, 'plate'-like ice crystals with a characteristic single-scattering phase function $\mathcal{P}$ were also considered. To estimate ΔF of young contrails, which primarily consist of near-spherical ice crystals (Goodman et al., 1998; Lawson et al., 1998; Gayet et al., 2012), the 'droxtal' parameterization after Yang et al. (2013) was added as a third choice. The three different ice habits can be interpreted as representing different stages in the temporal evolution of contrails.

- Aircraft in situ observations of young (t < 120 s) contrails showed that these consist of ice crystals with diameters up to a few micrometers (Petzold et al., 1997; Sassen, 1997; Schumann, 2002). Shortly thereafter these ice crystals grow in size and reach ice crystal radius r_{eff} between 2 and 5 μm (Jeßberger et al., 2013; Bräuer et al., 2021). The majority of ice crystals in older (t > 120 s) contrails and cirrus have r_{eff} between 10 and 150 μm (Krämer et al., 2020), while developed cirrus can be composed of ice crystals with diameters larger than 150 μm (Schröder et al., 2000). The conducted simulations cover only the lower range of the crystal size spectrum due to limitation in the provided ice optics parameterizations. Our simulations range from 5 to 45 μm for all three shapes and, therefore, focus on young contrails and cirrus.

The crystal / particle size distribution (PSD) is defined such that $n(\mathrm{r})\mathrm{d}r$ represents the number of cloud droplets or ice crystals in a cloud with a size between r and $r+\mathrm{d}r$. The PSD of liquid water and ice clouds is typically represented by a gamma distribution of the form:

$$n(r) = N_0 \cdot r^{\mu} \cdot \exp\left(-\Lambda \cdot r\right), \tag{5}$$

e.g., by Hansen and Travis (1974) or Petty and Huang (2011). N_0 is a constant factor, which itself results from the choice of the parameters in Eq. 5 that are given by the slope Λ and dispersion μ by:

$$\Lambda = \frac{1}{r_{\mathrm{eff}} \cdot \nu_{\mathrm{eff}}}; \mu = \frac{1 - 3 \cdot \nu_{\mathrm{eff}}}{\nu_{\mathrm{eff}}} \tag{6}$$

(Deirmendjian, 1962; Petty and Huang, 2011). The calculation of ν_{eff} is detailed in Eq. 15 of the paper by Petty and Huang (2011). In libRadtran, μ is set to unity, while N_0 and μ are found iteratively such that the PSD yields the mean r_{eff} (Emde et al., 2016).

Multiple definitions for the effective crystal radius r_{eff} exist in the case of non-spherical crystals. Here we follow the definition from Yang et al. (2000), Key et al. (2002), and Baum et al. (2005, 2007), which describe D_{eff} and r_{eff} of a non-spherical ice crystal population as:

$$D_{\mathrm{eff}} = 2 \cdot r_{\mathrm{eff}} = \frac{D_{\mathrm{V}}^3}{D_{\mathrm{A}}^2}, \tag{7}$$

with D_{V} the diameter of a spherical crystal with the same average volume as the ice crystal and D_{A} the diameter of a spherical crystal with the same projected area as the ice crystal. D_{A} is defined by:

$$D_{\mathrm{A}} = 2 \cdot r_{\mathrm{A}} = 2 \cdot \left(\frac{A}{\pi}\right)^{1/2} \tag{8}$$

and D_{V} is given by:

$$D_{\mathrm{V}} = 2 \cdot r_{\mathrm{V}} = \left(\frac{6 \cdot V}{\pi}\right)^{1/3}, \tag{9}$$

where V and A are the average volume and projected area of the crystal population, respectively. In practical application, the relationship between r_{eff} and D_{A} as well as D_{V} is derived from in situ observations for a given crystal shape. The original ice optical properties from Yang et al. (2000) and Yang et al. (2013) are post-processed by weighting the size dependent single-scattering phase function with the gamma distribution (Emde et al., 2016). Examples of phase functions $\mathcal{P}$ for four different crystal shapes and their characteristic features are visualized in Appendix C.

- Within libRadtran clouds are defined by their geometric thickness Δz, r_{eff}, and ice water content IWC. Typical IWC of contrails and in situ cirrus can range from 10^{-5} to 0.2 $\mathrm{g\,m^{-3}}$ as found during the Mid–Latitude Cirrus campaign (Luebke et al., 2016; Krämer et al., 2016, 2020). For our simulations, we span a similar range of IWC from $15 \cdot 10^{-4}$ to 0.1 $\mathrm{g\,m^{-3}}$.

Table 2. Basic model configuration and selected settings.

Model configuration	Selected value / setting
Radiative transfer solver	fdisort2 (Stamnes et al., 2000)
Number of streams	16
Extraterrestrial solar spectrum	Kurucz (1992)
Wavelength range	0.3–3.5 μm (solar) & 3.5–75 μm (thermal-infrared)
Molecular absorption	Fu and Liou (1992, 1993)
Ice properties	Yang et al. (2000)
Ice habit	aggregates, plates, droxtals
Output altitude	15 km = TOA, 1 km resolution

Table 3. Simulated parameter space (range), actual values selected (steps) and number of values selected.

Model parameter	Symbol	Range	Steps	
Solar zenith angle (°)	θ	0–70	0, 10, 30, 50, 70	5
Ice water content ($\mathrm{g\,m^{-3}}$)	IWC	$15 \cdot 10^{-4}$–0.1	0.0015, 0.003, 0.006, 0.012, 0.024, 0.05, 0.1	7
crystal effective radius (μm)	r_{eff}	5–45	5, 15, 30, 45	4
Cirrus temperature (K)	T_{ice}	223–243	223, 233, 243	3
Surface albedo	α_{srf}	0–1	0, 0.15, 0.3, 0.6, 1.0	5
Surface temperature (K)	T_{srf}	233–313	233, 273, 313	3
Atmosphere profiles	-	US Standard atmosphere, tropical, subarctic winter (Anderson et al., 1986)	-	3
Second cloud layer optical depth	τ_{wc}	0–20	0, 1, 5, 10, 20	5
Ice crystal shapes	-	aggregates, droxtals, plates		3
			Total number of combinations:	94,500

- The parameter sensitivity study is complemented by investigating the influence of a second cloud layer, with a cloud base at 3 km. In case of the subarctic winter profile the temperature at 3 km is below freezing but it is assumed that the cloud still consists of super-cooled droplets. The optical depth τ_{wc} of the liquid water cloud is varied between 0 and 20 at 550 nm wavelength. Within the RT simulations the optical properties of liquid water clouds are represented by pre-calculated Mie tables (Mie, 1908; van de Hulst, 1981).

An overview of the model configuration is given in Table 2 and the input parameter space is listed in Table 3. An example libRadtran input-file is provided as supplementary document.

https://doi.org/10.5194/egusphere-2023-155
Preprint. Discussion started: 3 February 2023

Table 4. List of variables that are provided in the NetCDF. The output is provided at TOA located at 15 km altitude.

Long name	Variable name	Unit
Downward solar total (direct + diffuse) irradiance	*Fdn_sol*	$\mathrm{W\,m^{-2}}$
Upward solar irradiance	*Fup_sol*	$\mathrm{W\,m^{-2}}$
Solar cloud radiative effect	*RF_sol*	$\mathrm{W\,m^{-2}}$
Thermal-infrared cloud radiative effect	*RF_tir*	$\mathrm{W\,m^{-2}}$
Net radiative effect	*RF_net*	$\mathrm{W\,m^{-2}}$
Ice cloud optical thickness	τ	-

For each of the three simulated ice crystal shapes a NetCDF file is provided (Wolf et al., 2023). The files include ice cloud optical thickness τ_{ice}, the simulated upward and downward irradiances F at TOA (with and without the presence of the ice cloud), and the calculated ice cloud radiative effect ΔF (solar, TIR, net). An overview of all variables provided in the NetCDF files are given in Table 4. The data set allows the user to extract ΔF values for their parameter combinations. The available cloudy and cloud-free irradiances further allow to calculate the cirrus RE by scaling the 'cloudy' RE with the required cloud cover. This serves as a first-approximation because, as 3D effects are neglected.

2.3 Relationship between effective radius, ice water content, crystal number concentration, and cloud optical thickness

Assuming spherical crystals the IWC of an ice cloud is calculated as:

$$\mathrm{IWC} = \frac{4}{3} \cdot \pi \cdot \rho_{\text{ice}} \cdot \int_0^\infty n(r) \cdot r_{\text{vol}}^3 \cdot \mathrm{d}r \tag{10}$$

with $\rho_{\text{ice}} = 917\ \mathrm{kg\,m^{-3}}$ the density of ice, $n(r)$ the PSD, and r_{vol} the volumetric radius. Rearranging Eq. 10 leads to the ice crystal number concentration of:

$$N_{\text{ice}} = \frac{3 \cdot IWC}{4 \cdot \pi \cdot \rho_{\text{ice}} \cdot r_{\text{vol}}^3 \cdot \beta}. \tag{11}$$

By adding a correction factor β the non-spherical shape of ice crystals is taken into account. Yang et al. (2003) determined that the volume ratio of a crystal with respect to a circumscribing sphere reaches a maximum value of 0.7 for droxtals, which we use in the following. One has to keep in mind that the resulting N_{ice} represents a lower boundary as β is smaller than 0.7 for all other ice crystal shapes. Equation 11 can also be used for liquid water clouds setting $\beta = 1$ and using the liquid water density $\rho_{\text{liq}} = 1000\ \mathrm{kg\,m^{-3}}$.

2.4 Blackbody emission

The RT in the TIR is primarily driven by the surface temperature T_{srf} and the (ice) cloud temperature T_{ice} with the latter one being directly linked to the vertical location of the cloud in the atmosphere and the atmospheric temperature profile. In a first order approximation, the emitted irradiance of a blackbody can be calculated by the Stefan–Boltzmann-law:

$$F = \sigma \cdot \epsilon \cdot T^4, \tag{12}$$

which is obtained by integrating the Planck function over all wavelengths and $2{\cdot}\pi$ of a hemispheric solid angle. In Eq. 12 the Stefan–Boltzmann-constant is represented by σ in units of $\mathrm{W\,m^{-2}\,K^{-4}}$ and the emissivity ϵ of a body. While sufficiently geometrical thick liquid and ice water clouds might be treated as black bodies with $\epsilon \approx 0.95$, geometrically thin clouds with low liquid or ice water path act as gray bodies. The cirrus emissivity of such thin clouds might be approximated by:

$$\epsilon = 1 - \exp\left(-\zeta \cdot CWP\right), \tag{13}$$

with factor $\zeta = 0.144\ \mathrm{m^2\,g^{-1}}$ from Stephens (1978) and the cloud water path CWP in units of $\mathrm{g\,m^{-2}}$ (Lohmann and Roeckner, 1995). Nevertheless, the maximum of emitted radiation might be estimated on basis of a black body, knowing that the truly emitted radiation is smaller. Equation 12 therefore states the total irradiance emitted by an object is proportional to T^4. Using Eq. 12, ΔF_{tir} can be approximated by:

$$\Delta F_{\mathrm{tir}} \approx F_{\mathrm{srf}} - F_{\mathrm{cld}} = \sigma \cdot \epsilon \cdot \Delta T^4 = \sigma \cdot \epsilon \cdot (T^4_{\mathrm{srf}} - T^4_{\mathrm{ice}}). \tag{14}$$

Consequently, ΔF_{tir} of an ice cloud results from the temperature difference between surface (T_{srf}) and cirrus (T_{ice}). When a second cloud layer is involved and the liquid water cloud cloud is optically opaque in the TIR then T_{srf} is replaced by the temperature $T_{\mathrm{cld,wc}}$ of the underlying cloud layer.

3 Results

Separating the intertwined dependencies of ΔF on the input parameters is key to understanding the cirrus and contrail RE. To provide a first overview how r_{eff} and IWC determine the cloud optical and microphysical properties, Fig. 1a–d illustrates the dependence between N_{ice} and τ_{ice} as a function of r_{eff} and IWC. While N_{ice} is approximated by Eq. 11, τ_{ice} is directly diagnosed by libRadtran.

Figure 1a visualizes the linear dependency of N_{ice} on IWC and a dependency on the power of -3 on r_{eff}. The largest N_{ice} values result from the smallest ice crystals sizes ($r_{\mathrm{eff}} < 20\ \mu$m), particularly in combination with large IWC. For those combinations (small r_{eff} and large IWC) N_{ice} is most sensitive to r_{eff}, which is indicated by the narrowing contour lines that align along the x-axis. For a constant r_{eff} value of 5 μm, the estimated N_{ice} ranges from 1 to over 100 cm^{-3}. Such concentrations of $N_{\mathrm{ice}} > 100\ \mathrm{cm^{-3}}$ are rarely observed in natural cirrus though they can occur in contrails and contrail-induced cirrus (Krämer et al., 2016). Generally smaller N_{ice} and a reduced sensitivity is found for $r_{\mathrm{eff}} > 20\ \mu$m, where N_{ice} ranges below 1 cm^{-3}.

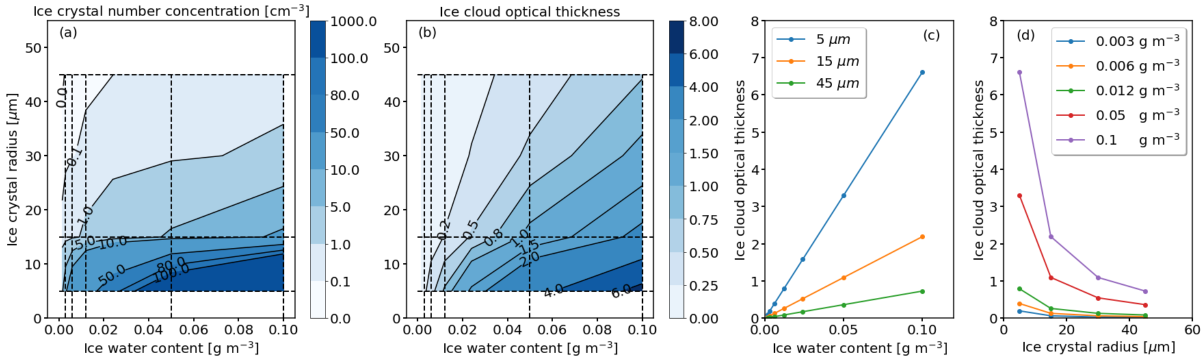

Figure 1. (a–b) Ice crystal number concentration N_{ice} (in cm^{-3}) and cloud optical thickness τ at 640 nm wavelength as a function of ice water content IWC (in $\mathrm{g\,m}^{-3}$) and effective crystal radius r_{eff} (in μm). **(c–d)** Cross-sections along lines of constant r_{eff} or IWC that are indicated as dashed lines in panel a or b, respectively.

The observed dependencies of N_{ice} presented in Fig. 1a are also found in the distribution of the ice cloud optical thickness τ_{ice} at 640 nm given in Fig. 1b. Following lines of constant r_{eff} (Fig. 1c), the increase in IWC corresponds to a linear increase in N_{ice} and, therefore, to a gain in the total scattering and absorption particle cross-sections. The absorption of radiation by liquid water and ice (as characterized by the complex refractive index) at 640 nm wavelength is weak and therefore scattering is dominating τ_{ice}. Alternatively, going along lines of constant IWC towards larger r_{eff} leads to a decrease in N_{ice} and a related decrease of the total scattering particle cross-section (cloud albedo effect, Fig. 1d). This effect is most effective for larger IWC (optically thick clouds) and is less pronounced for clouds with smaller IWC.

Going beyond these dependencies, the impact of each parameter is estimated by varying each of them in turn, while the remaining parameters are kept at a fixed reference value. Modifying each parameter separately can be interpreted as a type of a sampling, by averaging all unfixed values, to 'project' ΔF onto the one-dimensional space. The impact of each parameter is quantified by the minimum and maximum RF. We define the full range of ΔF by:

$$R_{\Delta \mathrm{F}} = max\{\Delta F\} - min\{\Delta F\}, \tag{15}$$

with $max\{\Delta F\}$ and $min\{\Delta F\}$ the maximum and minimum of ΔF across the 94,500 combinations of input parameters, respectively. As $R_{\Delta \mathrm{F}}$ is susceptible to outliers, we further characterize the width of a distribution by the inter-quartile range, which is defined as the difference between the 75th ($Q_{75\%}$) and 25th ($Q_{25\%}$) percentile of ΔF:

$$Q_{\Delta \mathrm{F}} = Q_{75\%}(\Delta F) - Q_{25\%}(\Delta F) \tag{16}$$

A reference cloud is created by selecting minimum or maximum values from the parameter space given by $\theta = 0°$, $T_{\mathrm{ice}} = 223$ K, $\alpha_{\mathrm{srf}} = 0$, $T_{\mathrm{srf}} = 313$ K, r_{eff} = 45 μm, and τ_{wc} = 0 (no liquid water cloud). An exception is the selected IWC, which is set to a medium value of $0.024\,\mathrm{g\,m}^{-3}$. This is done to ensure that τ_{ice} of the reference case, considering our fixed $\Delta z = 0.2\,\mathrm{km}$ and reference $r_{\mathrm{eff}} = 45$ μm, is 0.18 at 640 nm wavelength, which is representative for contrails and young cirrus. Figure 2a–c

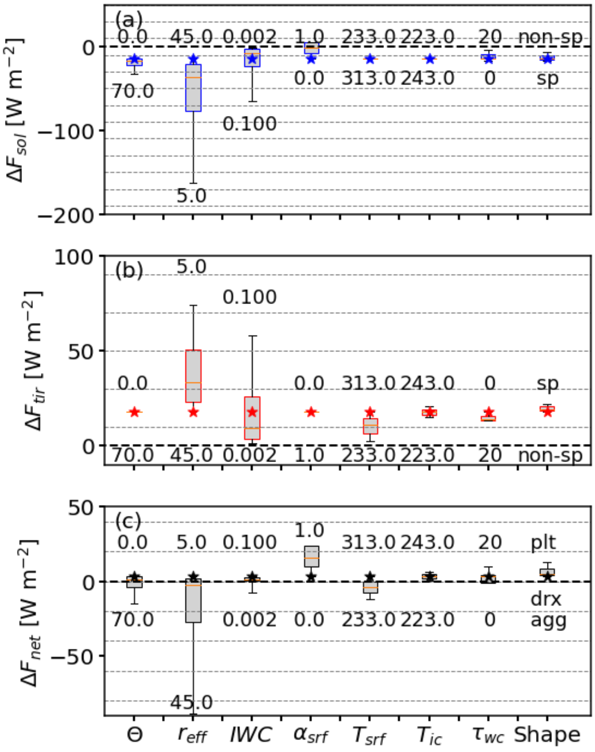

Figure 2. (a–c) Box and whisker plot of solar, TIR, and net ΔF due to the variation of the parameters indicated as the x-axis. The boxes represent the 25 % and 75 %-percentiles and the whiskers indicate the minimum and maximum values. Median values are given in each box by horizontal, orange lines. The stars indicate the reference case with $\theta = 0°$, r_{eff} = 5 μm, IWC = 0.024 g m^{-3}, $\alpha_{\mathrm{srf}} = 0$, T_{srf} = 313 K, z = 13 km, and τ_{wc} = 0. Minimum and maximum of the parameter ranges are given by the numbers. Plot idea adapted from Meerkötter et al. (1999).

shows solar, TIR, and net ΔF, respectively. First, the influence of variations in θ is investigated in order to sample the diurnal cycle and its variation as a function of latitude. For the all Sun geometries, ΔF_{sol} is negative and, therefore, the cirrus has a cooling effect in the solar spectrum on the atmosphere-surface system. ΔF_{sol} intensifies (i.e., becomes more negative) with increasing θ as the length of the photon path, $s = \Delta z / \cos\theta$, through the cloud increases, which is accompanied by enhanced scattering (and thus upward directed scattering) of the incoming radiation. In addition, a lower fraction of the incident radiation is scattered towards the surface but scattered upward back into space. This is due to the strong forward peak in the ice crystal phase function $\mathcal{P}$ that decreases sharply for $\Theta > 10°$ (see in Appendix Fig. C1). Variations in θ lead to ΔF_{sol} between -32.7 and -14.6 W m^{-2}. As expected, ΔF_{tir} is unaffected by the Sun position with a constant ΔF_{tir} = 17.9 W m^{-2}. The resulting sensitivity of ΔF_{net} is driven by ΔF_{sol} with ΔF_{net} between -14.8 and 3.3 W m^{-2}. During nighttime there is no contribution from ΔF_{sol} leading to a constant, positive ΔF_{net} = 17.9 W m^{-2} (leading to a warming).

https://doi.org/10.5194/egusphere-2023-155
Preprint. Discussion started: 3 February 2023

As expected, variations in r_{eff} have the largest effect on the solar, TIR, and net ΔF, as N_{ice} relates to r_{eff} by the power of -3 (see Eq. 11). Increasing r_{eff} from 5 to 45 μm leads to ΔF_{sol} between -162.5 and -14.6 W m^{-2}. The distribution of ΔF_{tir} has a minimum and maximum of 17.9 and 74.2 W m^{-2}, respectively. ΔF_{sol} dominates ΔF_{tir} and results in values of ΔF_{net} ranging from -88.3 to 3.3 W m^{-2}.

Variations in IWC affect solar, TIR, and net ΔF. Generally, an increase in IWC (increase in τ_{ice} for fixed r_{eff}), enhances total scattering and absorption particle cross-section and, therefore, intensifies the cooling in the solar (more negative ΔF, cloud albedo effect) and the TIR heating (more positive ΔF). ΔF_{sol} ranges from -65.1 to -0.9 W m^{-2}, with $\Delta F_{\mathrm{sol}} = -14.6$ W m^{-2} obtained for the reference IWC. The distribution of ΔF_{tir} spans values between 1.2 and 57.8 W m^{-2}, leading to ΔF_{net} from -7.3 to 3.3 W m^{-2}. The given ΔF ranges, by varying IWC, assume r_{eff} = 45 μm. Smaller r_{eff} increase the range of solar, TIR and net ΔF.

Variations in α_{srf} impact only the solar spectrum, as expected, with ΔF_{sol} between -14.6 and 5.9 W m^{-2}. The most negative RE appears over non-reflective surfaces and decreases with increasing α_{srf}, due to the decrease in contrast between the surface and the cirrus. In cases where α_{srf} exceeds the reflectivity of the cloud, ΔF_{sol} becomes positive. For the optical thin reference cloud this is the case over a fully sea ice covered area with $\alpha_{\mathrm{srf}} \approx 1$. The TIR component remains unaffected with $\Delta F_{\mathrm{tir}} = 17.9\,\mathrm{W\,m^{-2}}$. Together with the decreasing cooling effect in the solar, the warming in the TIR dominates and leads to a net warming cirrus with ΔF_{net} ranging between 3.3 and 23.8 W m^{-2}.

Varying surface temperature T_{srf} or cirrus temperature T_{ice} (related to cloud base altitude), ΔF_{sol} remains almost constant with a minimum and maximum ΔF_{sol} for both parameters of -14.6 and -14.4 W m^{-2}, respectively. These differences are due to changes in molecular absorption, which result from the variations in the relative humidity profile as the profile depends on the selected T_{srf}. A noticeable effect is found for ΔF_{tir}, which is impacted by variations in T_{ice} and T_{srf}. While decreasing T_{ice} from 243 to 223 K lowers ΔF_{tir} from 20.6 to 15 W m^{-2}, a decrease in T_{srf} from 313 to 233 K reduces ΔF_{tir} from 15 to 0.2 W m^{-2}. Consequently, ΔF_{tir} determines the response of the resulting ΔF_{net}, which spans from 6 to 0.2 W m^{-2} for T_{ice} and -14.2 to 0.5 W m^{-2} for T_{srf}. The greater influence of T_{srf} on ΔF_{tir} and ΔF_{net} can be explained simply by the greater variation of the input.

A second cloud layer is considered by inserting a liquid water cloud with a cloud base altitude $z_{\mathrm{base}} = 3\ \mathrm{km}$ and a geometric thickness $\Delta z = 200\ \mathrm{m}$. Figure 2 shows that this second cloud influences both components ΔF_{sol} and ΔF_{tir}. Generally speaking, the liquid water cloud enhances the fraction of solar, upward directed radiation compared to a dark surface. With increasing τ_{wc} (increase in LWC) α_{cld} exceeds α_{srf}, which lowers the albedo contrast between the ice cloud and the surface for most of the parameter combinations. This minimizes solar RE and leads to a minimum of -16.2 W m^{-2} and a maximum of -3.6 W m^{-2}. For the TIR part the increase in LWC masks the influence of the underlying surface by absorbing the upward TIR radiation from the surface and re-emitting radiation at the liquid water cloud temperature. This leads to ΔF_{tir} between 10.5 and 15 W m^{-2}. The resulting ΔF_{net} is almost equally impacted by the two wavelength ranges and the distribution is characterized by a minimum and maximum of -3.7 and 6.9 W m^{-2}.

The parameter study is complemented by investigating the effect of prescribing three different ice crystal shapes. The variation in ΔF_{sol} due to the transition from almost spherical (droxtals) to non-spherical crystals (aggregates) leads to a relative

https://doi.org/10.5194/egusphere-2023-155
Preprint. Discussion started: 3 February 2023

change in ΔF_{sol} that is, in terms of RE, comparable to a variation in θ. The strongest cooling effect (negative ΔF_{sol}) is found for droxtals with -16.9 W m^{-2} and decreases for aggregates and plates to -15 and -6.8 W m^{-2}, respectively. Ice crystal shape also impacts ΔF_{tir}. Aggregates lead to ΔF_{tir} of 17.9 W m^{-2}, while plates and droxtals can cause a ΔF_{tir} of 20.2 and 22.7 W m^{-2}, respectively. Consequently, the largest ΔF_{net} with 13.4 W m^{-2} is found for plates and followed, in decreasing order, by droxtals and aggregates with 5.8 and 3.3 W m^{-2}, respectively. As mentioned in the introduction, the uncertainty in the ice crystal shape causes uncertainties in the calculated ΔF. Nevertheless, using three different ice crystal shapes for the irradiance simulations shows that the shape-specific scattering properties are of lesser importance compared to other parameters like the ice crystal size (distribution), the IWC, or surface properties.

It must be emphasized that the presented ΔF_{net} is representative for daytime situations only, where θ is between 0° and 70°. In the absence of solar illumination during nighttime, the net effect is entirely determined by and equal to ΔF_{tir}, which is positive (warming effect) in all simulation cases. Accordingly, all simulated cloud cases do have a net warming effect at night. For a more in-depth analysis, the subsequent plots focus on the impact of each individual parameter.

3.1 Sensitivity on ice crystal shape

Scattering and absorption by an ice crystal is characterized by its shape, orientation, size, complex refractive index of ice, and the wavelength of the incident light. To some extent, the dependence on the shape can be partly condensed into the knowledge of the crystal aspect ratio, which is defined as the ratio of the width to the length of a non-spherical crystal (Macke et al., 1998). For non-spherical crystals the effective crystal diameter or radius (Eq. 7) is smaller than the geometrical crystal diameter or radius. Considering small crystals with $r_{\mathrm{eff}} \approx 50\ \mu\mathrm{m}$, the aspect ratio is largest for spheres and followed, in descending order, by droxtals, solid columns, spheroids, hallow columns, plates, and aggregates (Yang et al., 2005). In this order, the crystals become less effective in the interaction with incident radiation for the same maximum dimension. Consequently, the assumption of an ice crystal habit, related ice crystal phase function (Fig. C1), and the ice crystal size distribution are vital information to estimate the ice cloud RE. One caveat of RT simulations in ice clouds is the uncertainty about the dominating ice crystal shape, which is commonly unknown and, therefore, a general ice habit has to be assumed. The assumption of an ice crystal shape represents a fundamental uncertainty in the understanding of ice clouds (Kahnert et al., 2008).

Subsequently, the shape-effect is quantified using Eq. 15 and relative difference in ΔF are given with respect to crystals with the same r_{eff} in relation to the ΔF simulated for aggregates. Figure 3a–c show ΔF_{sol} as a function of IWC, separated for crystal shape, r_{eff}, and three selected θ. For simplicity α_{srf} and τ_{wc} are set to zero in these simulations.

The strongest ΔF_{sol} is found for plate-like crystals with $r_{\mathrm{eff}} = 5\,\mu\mathrm{m}$ that are illuminated by the Sun at zenith ($\theta = 0°$, Fig. 3a). A lower cooling effect in the solar spectrum is found for aggregates and droxtals with same r_{eff}. The order of ΔF_{sol} changes with increasing r_{eff} and the strongest solar cooling is identified for aggregates and followed by droxtals. The re-ordering in the intensity of ΔF_{sol}, by keeping θ constant, is traced back to the size dependence of the absorption particle cross-section and $\mathcal{P}$ as can be seen in Fig. C1.

The spread in ΔF_{sol} across crystals shapes with the same r_{eff} and IWC can be interpreted as the uncertainty in ΔF_{sol} due to the ice habit. One has to keep in mind that the differences partially result from deviating crystal size distributions as these

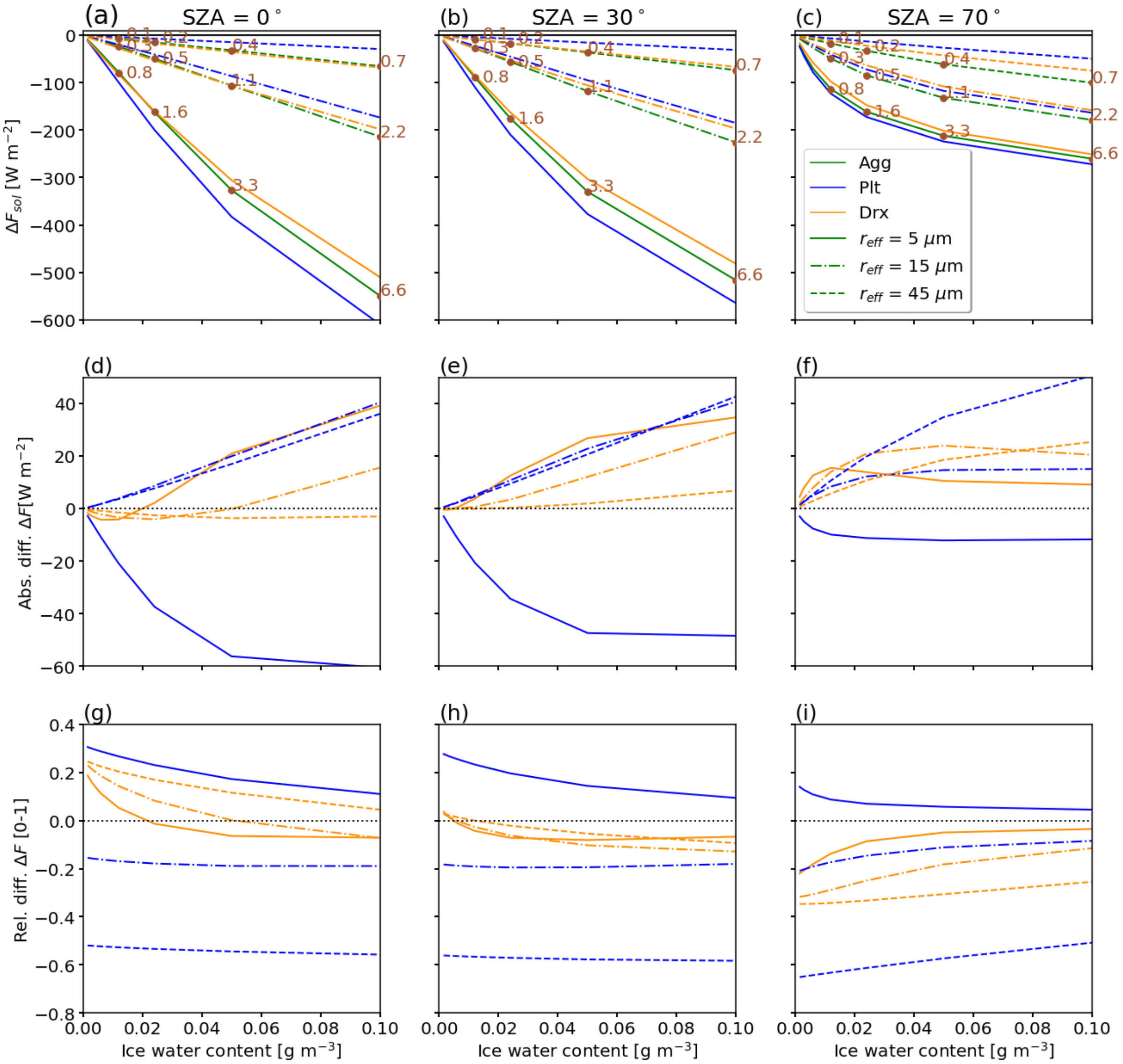

Figure 3. (a–c) Solar radiative effect ΔF_{sol} as a function of IWC for three values of θ of 0°, 30°, and 70°. Three ice crystal radii of 5 (solid), 30 (dash-dot), and 48 μm (dashed) are indicated. The ice crystal shape is color-coded. **(d–f)** show absolute difference and **(g–i)** relative difference between ΔF_{sol} of droxtals and plates with respect to aggregates with the same crystal radius.

depend on the selected crystal shape that goes into the calculation of the crystal number $n(r)$ (Eq. 5). Nevertheless, Macke and Großklaus (1998) showed that the crystal habit is the main driver and the actual ice particle size distribution has only a minor effect.

To quantify the deviations, panels 3d–f show absolute and panels 3g–i present relative differences of ΔF_{sol} of droxtals (green) and plates (blue) with respect to aggregates. In general, the largest absolute and smallest relative deviations are found for the optically thickest clouds (highest IWC). Among all θ the largest absolute ranges, expressed in $R_{\Delta \mathrm{F,sol}}$, are found between aggregates and plates, where $R_{\Delta \mathrm{F,sol}}$ reaches up to -60 W m^{-2} (5 μm, $\theta = 0°$, $\tau_{\mathrm{ice}} = 7.1$), corresponding to a relative difference of 15 %. Relative deviations reach even larger values, e.g., when the cloud is optically thin and ΔF_{sol} is small. In case of plates the relative deviations range from 35 % (5 μm) to -58 % (48 μm). With increasing θ the absolute ranges in ΔF_{sol} become smaller. Another characteristic of $R_{\Delta \mathrm{F,sol}}$ is the steep slope for $\theta = 0°$ over the entire range of IWC. For illumination geometries with the Sun closer to the horizon, particularly $\theta = 70°$, the behavior of absolute range in ΔF_{sol} is characterized by a rapid increase and convergence towards a maximum. At a certain IWC and related τ_{ice}, the slant light path and cloud-radiation interactions are dominated by multiple scattering that suppresses single-scattering effects of individual ice habits, hence, reducing the absolute and relative difference resulting from the choice of the ice habit.

Next, we consider the solar, TIR, and net ΔF at $\theta = 30°$ (Fig. 4). The left most column for ΔF_{sol} is identical with the center column in Fig. 3. In the TIR, the largest ΔF_{tir} is generally found for smallest crystals (5 μm) and highest IWC in decreasing order from droxtals, plates, and aggregates. The order remains constant of all crystal sizes. The largest ΔF_{tir} range of 10 W m^{-2} is found for clouds with intermediate IWC between 0.02 and 0.06 g m^{-3} caused by droxtals. For thin clouds IWC < 0.04 g m^{-3} the largest relative differences of 38 % appear, e.g., droxtals with 15 μm, while deviations of 8 to 10 % are calculated for optically thick clouds containing plate-like crystals.

In case of IWC = 0.1 g m^{-3}, ΔF_{sol} is larger by a factor of five than ΔF_{tir} and, therefore, dominates resulting ΔF_{net} (Figure 4c,f). In general, the range of ΔF_{tir} increases and the relative differences decrease towards the maximum of simulated IWC. In this case the value range of ΔF_{tir} is between -40 (10 %) and 40 W m^{-2} (10 %) for plates and droxtals with sizes of 5 μm, respectively.

It has to be added that, as shown in Fig 2, the shape assumption has only second-order implications of the RE compared to other parameters. Nevertheless, the shape-effect is of high importance in case of radiance simulations and cloud remote sensing applications.

3.2 Sensitivity to solar zenith angle and surface albedo

Variations in θ are caused by the diurnal and seasonal cycle of the Earth, or variations along the longitude at a given time. Figure 5a shows solar ΔF_{sol} at $\theta = 0°$ with distributions ranging from -554.7 (high IWC) to 35.7 W m^{-2} (high α_{srf}). For all simulated θ, the median values range from -4 to -7.1 W m^{-2} with an intensification of ΔF_{sol} towards larger θ. The upper boundaries of ΔF_{sol} are shifted towards zero, which is a combination of three effects: i) a decreasing downward irradiance at TOA with increasing θ; ii) an increasing path length s through the cloud with increasing θ and accompanied scattering; and iii) an increased upward scattering with increasing θ as the light rays get slanted and a larger fraction of the forward peak is

https://doi.org/10.5194/egusphere-2023-155
Preprint. Discussion started: 3 February 2023

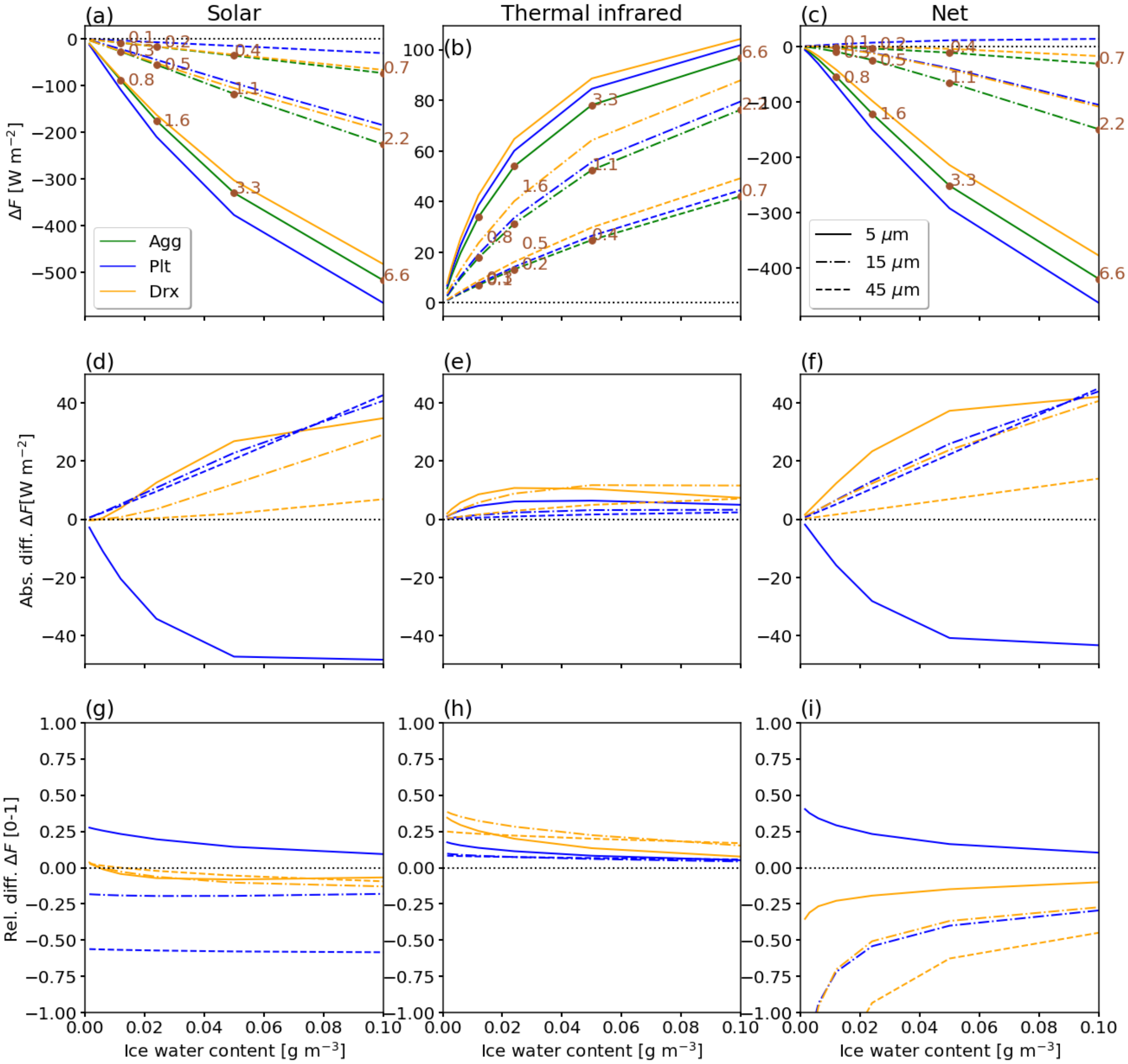

Figure 4. Same as Fig. 3 but for $\theta = 30^\circ$, and ΔF_{sol} (left), ΔF_{tir} (middle), and ΔF_{net} (right).

https://doi.org/10.5194/egusphere-2023-155
Preprint. Discussion started: 3 February 2023

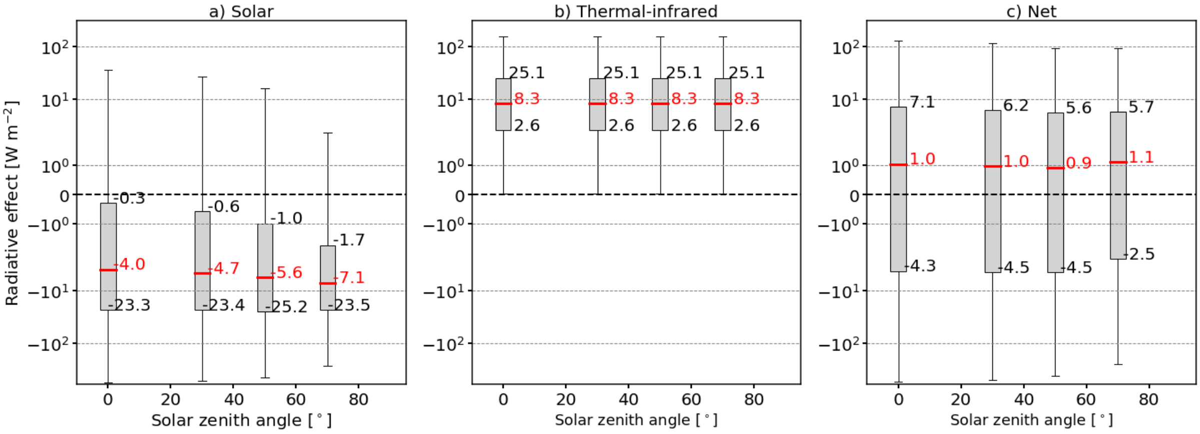

Figure 5. Box plots of **(a)** solar, **(b)** TIR, and **(c)** net ΔF as a function of the solar zenith angle θ. Median values are indicated in red, the 25 % – 75 % range is represented by the gray boxes, and the 10 % and 90 %-percentiles are given by the whiskers.

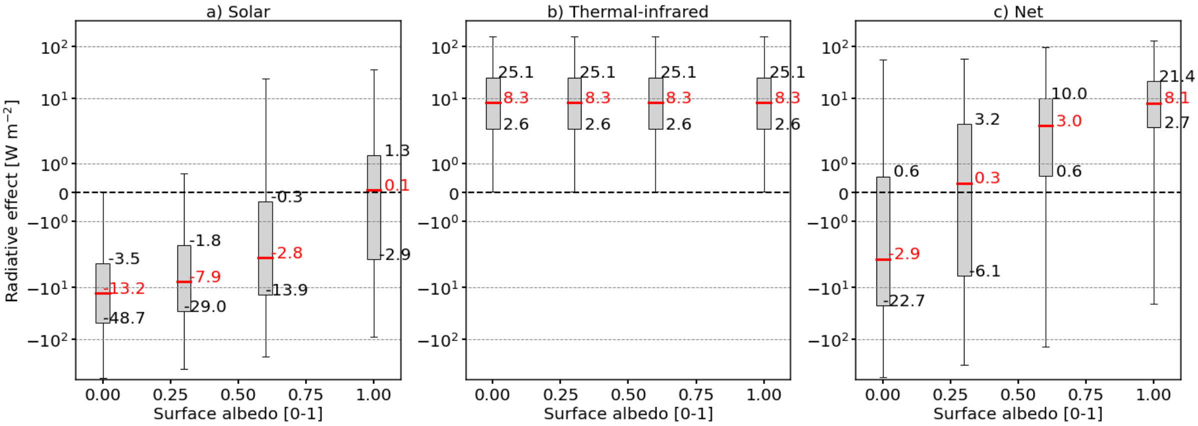

Figure 6. Same as Fig. 5 but as a function of the surface albedo α_{srf}.

directed upwards. Effects i) and ii) compete and are dominated by effect iii). The combination of effects i)–iii) also reduces the inter-quantile for larger θ and indicates a reduced influence of the other free parameters on ΔF_{sol}.

ΔF_{tir} is unaffected by changes in θ (Fig. 5b) with a constant median ΔF_{tir} of 8.3 W m^{-2}. The highest positive values of ΔF_{tir} (strongest warming effect) are found for clouds with maximal IWC. Resulting ΔF_{net}, given in Fig. 5c, is dominated by a warming in the TIR that leads to median ΔF_{net} around 1.0 W m^{-2}, with minimum ΔF_{net} of -526.5 W m^{-2} and maximum of 126.9 W m^{-2}. The reduced variability of ΔF_{sol} with increasing θ propagates into the distribution and variability in ΔF_{net}.

The influence of the underlying surface is shown in Fig. 6. For $\alpha_{\mathrm{srf}} = 0$ the surface absorbs the entire incident solar radiation creating the largest contrast between α_{srf} and the cloud albedo α_{cld}. As long as the surface is fully absorbing ($\alpha_{\mathrm{srf}} = 0$), all simulated cloud combinations are characterized by a cooling in the solar with ΔF_{sol} ranging from -554 to 0 W m^{-2}.

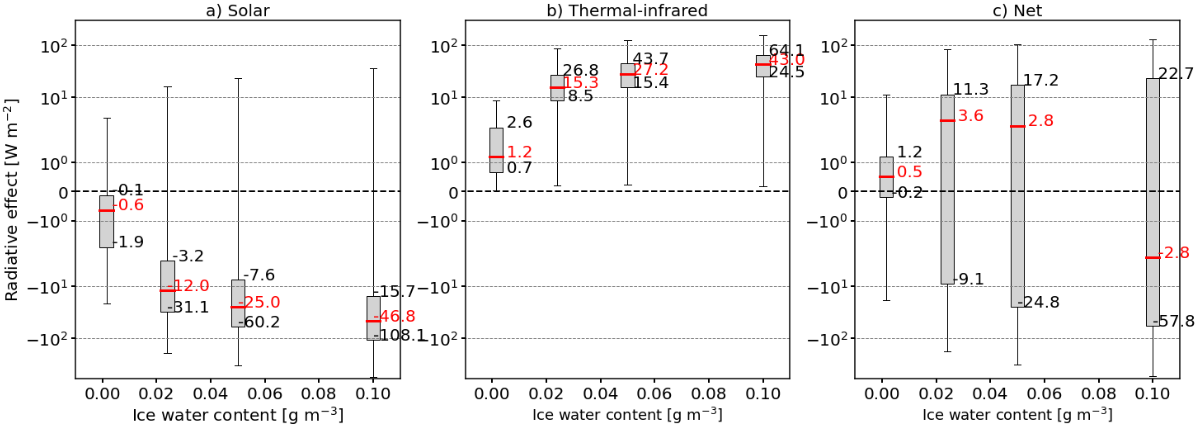

Figure 7. Same as Fig. 5 but as a function of ice water content IWC.

The cooling is reduced when the surface becomes more reflective and the contrast between surface and cloud is reduced, which shifts the distributions and their medians towards positive ΔF_{sol}. With α_{srf} approaching 0.66, around 25 % of the parameter combinations lead to a solar heating. This becomes even more pronounced towards $\alpha_{\mathrm{srf}} = 1$, where around 50 % of the simulations have a warming effect in the solar. ΔF_{tir} is unaffected and remains constant for all α_{srf} with a median at 8.3 W m^{-2}. Resulting ΔF_{net} is dominated by a net warming effect, indicated by mostly positive median values ranging from 0.3 W m^{-2} ($\alpha_{\mathrm{srf}} = 0.25$) to 8.1 W m^{-2} ($\alpha_{\mathrm{srf}} = 1$). An exception is $\alpha_{\mathrm{srf}} = 0$, where more than 50 % of the simulations lead to a net cooling with a median ΔF_{net} at -2.9 W m^{-2}.

3.3 Sensitivity on ice water content and ice crystal radius

As presented in Fig. 2, IWC is the primary factor that controls ΔF. For a constant crystal number concentration the increase in IWC leads to an increase in total particle scattering and absorption cross-sections, as well as r_{eff}. This enhances scattering and absorption along the light path though the cloud. Figure 7a reveals that with increasing IWC the median of ΔF_{sol} becomes more negative (intensification of the cooling effect in the solar part of the spectrum). The steepest increase is found for IWC < 0.04 g m^{-3}, while for IWC $\geq$ 0.04 g m^{-3} the solar cloud RE saturates. At the same time $Q_{\Delta F,sol}$ increases, indicating an enhanced sensitivity of ΔF_{sol} on the free parameters. The minimum and maximum of ΔF_{sol} result from clouds over highly reflective surface (α_{srf} = 1) and clouds containing crystals with the smallest r_{eff} = 5 μm.

For ΔF_{tir} the increase in IWC leads to an intensified warming effect (Fig. 7b). Again, this is caused by the increase in the total particle scattering and absorption cross-sections. Similar to ΔF_{sol}, the steepest increase appears for IWC < 0.04 g m^{-3}, while for larger IWC the medians approach an almost constant level and a further increase in IWC has only a limited effect on ΔF_{tir}. Beyond an IWC of 0.04 g m^{-3} the photon mean free path in the cloud becomes smaller than the geometric thickness of the cloud and a further increase in IWC (τ_{ice}) has an almost negligible impact on the cloud RE in the solar and TIR. The

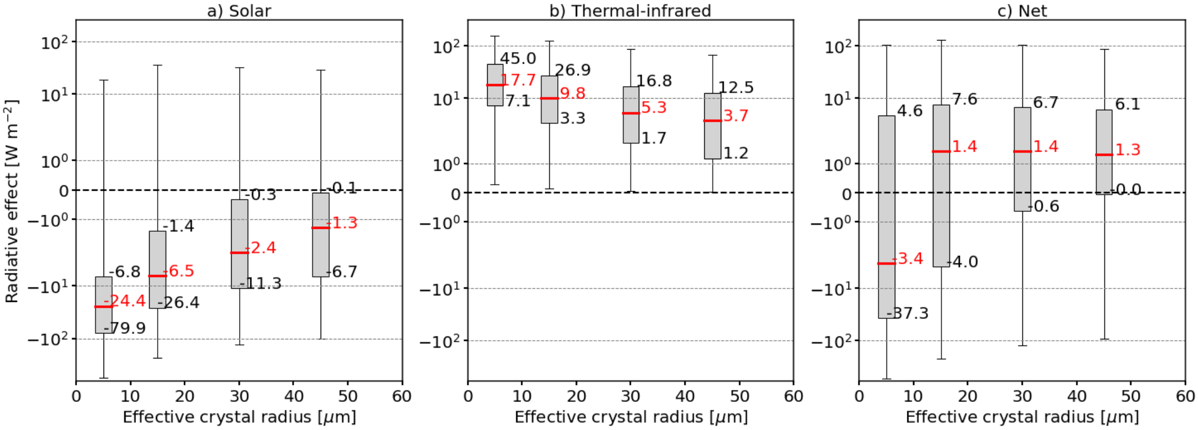

Figure 8. Same as Fig. 5 but as a function of effective crystal radius r_{eff}.

resulting ΔF_{net} (Fig. 7c) ranges from -526.5 to 126.9 W m^{-2} and is skewed to positive ΔF_{net} with median values between -2.8 and 3.6 W m^{-2}.

Figure 8 illustrates that cirrus with the smallest r_{eff} are associated with the most intense cooling effect in the solar, leading to ΔF_{sol} between -554.7 and 19.1 W m^{-2}. Small crystals and high number concentrations lead to higher α_{cld} in the solar compared to fewer and larger crystals (Stephens et al., 1990; Zhang et al., 1994). For the smallest crystals in the simulations a median value of -24.4 W m^{-2} is determined. For increasing crystal radius the cooling effect in the solar range decreases and tends towards a neutral solar RE (ΔF_{sol} = -1.3 W m^{-2}). Increasing r_{eff}, while keeping the IWC constant, is directly linked to a decrease in the ice crystal number concentration (cloud albedo effect). Clouds with larger r_{eff} are found to be less sensitive to the effect of the free parameters as the inter-quartile range decreases from $Q_{\Delta\mathrm{F,sol}}(r_{\mathrm{eff}} = 5\,\mu\mathrm{m}) = 73.1\,\mathrm{W\,m^{-2}}$ to $Q_{\Delta\mathrm{F,sol}}(r_{\mathrm{eff}} = 45\,\mu\mathrm{m}) = 6.6\,\mathrm{W\,m^{-2}}$. Similarly, the strongest TIR heating occurs for the smallest crystals as such small crystals have the largest emissivity (Stephens et al., 1990; Zhang et al., 1994). An increase in r_{eff} leads to a reduction in ΔF_{tir}, which is caused by the lower total particle scattering and particle absorption cross-sections. $Q_{\Delta\mathrm{F,tir}}$ for $r_{\mathrm{eff}} = 5\,\mu\mathrm{m}$ decreases from 37.9 to 11.3 W m^{-2}. Median values of ΔF_{net} indicate only a net cooling for $r_{\mathrm{eff}} = 5\ \mu\mathrm{m}$ with -3.4 W m^{-2}, whereby elsewhere a net warming is dominant with ΔF_{net} around 1.4 W m^{-2}. Simultaneously, $Q_{\Delta\mathrm{F,net}}$ decreases, which indicates the reduced impact of the remaining free parameters.

3.4 Multi-dimensional dependencies on θ, α_{srf}, r_{eff}, and IWC

The previous analysis aimed to sample the 8D-hypercube in a series of 1D–cross-sections to focus on the general distribution of ΔF that result from a single parameter. This likely masks dependencies of ΔF on specific parameter combinations that are closely interconnected. Subsequently, we focus on a detailed analysis, particularly in the solar wavelength range, to highlight the dependencies among Sun geometry, surface albedo, and cloud properties - namely r_{eff} and IWC.

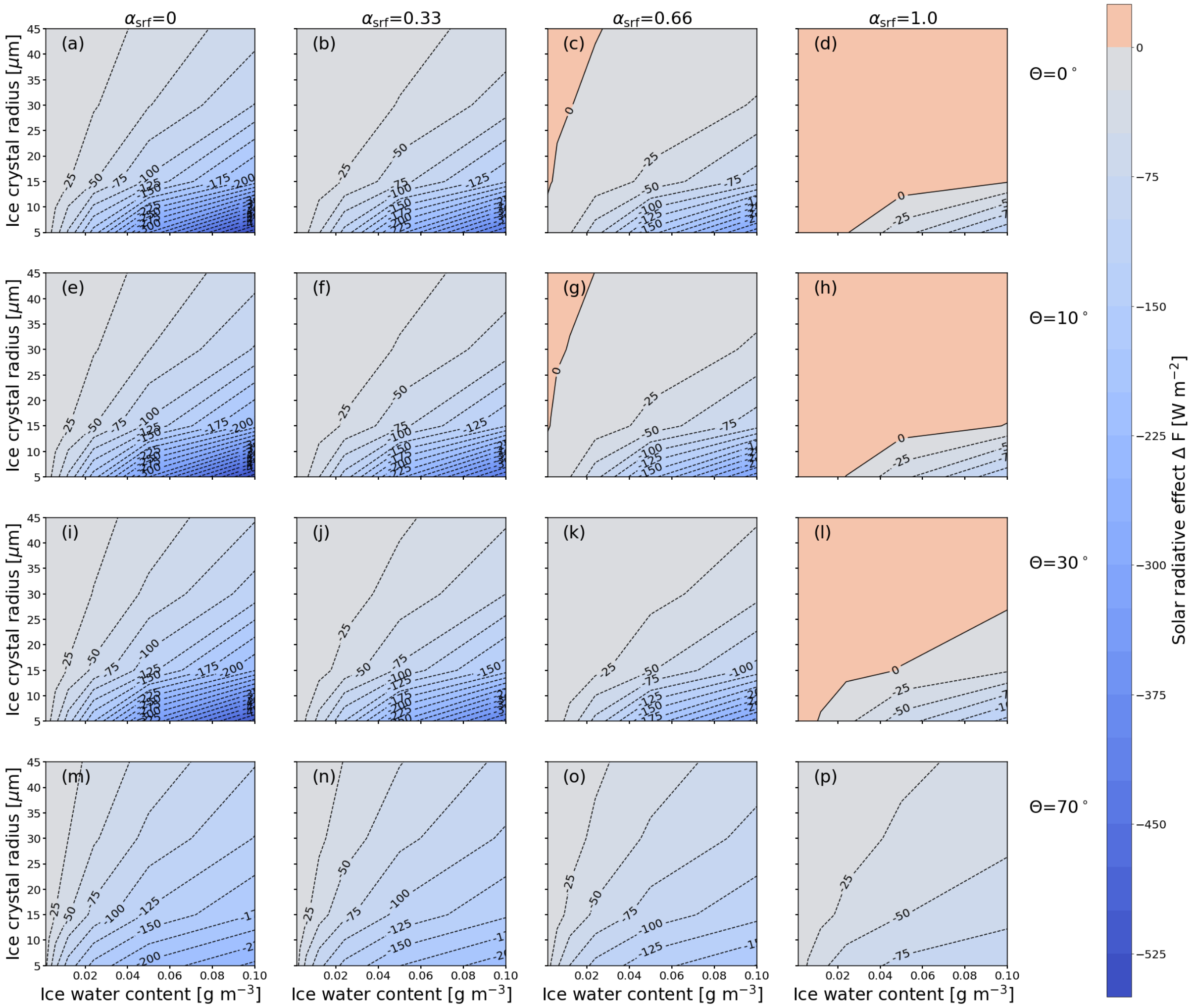

Figure 9. Solar cloud radiative effect ΔF_{sol} sampled into two-dimensional parameter space of ice water content IWC and effective radius r_{eff}. Each panel represents combinations of surface albedo α_{srf} at 550 nm and solar zenith angle θ. Blue values indicate negative ΔF_{sol} (cooling) and red values indicate positive (warming) ΔF_{sol}. The contour lines provide a direct measure of the sensitivity to the indicated parameters.

3.4.1 Solar

Figure 9 shows ΔF_{sol} as a function of IWC and r_{eff} for combinations of α_{srf} (column) and θ (row). Moving from the left to the right column the surface becomes more reflective (increasing α_{srf}) and going from the top to the bottom row the Sun approaches the horizon (increasing θ). The panels along the diagonal can be understood as a transition from the Equator ($\theta \approx 0°$, $\alpha_{\mathrm{srf}} \approx 0$) towards the Poles with low Sun ($\theta \approx 70°$) with an increase in sea ice cover ($\alpha_{\mathrm{srf}} \approx 1$).

https://doi.org/10.5194/egusphere-2023-155
Preprint. Discussion started: 3 February 2023

Figure 9a represents non-reflective surfaces and a Sun at the zenith. In these cases and focusing on ice crystals with $r_{\mathrm{eff}} >$ 20 μm the contour lines are well separated. A wide spacing of the contour lines indicates a low sensitivity of ΔF_{sol} on IWC and r_{eff}. In those regions ΔF_{sol} ranges from 0 to -80 W m^{-2} (cooling), with an intensification of ΔF_{sol} for decreasing r_{eff}. Simultaneously, the contour lines narrow and align with the x-axis, which indicates an increase in the sensitivity of ΔF_{sol}, particularly with respect to r_{eff}.

For the Sun at zenith and cirrus above reflective surfaces ($0 < \alpha_{\mathrm{srf}} < 1$), the sensitivity with respect to IWC and r_{eff} is generally reduced. This results from the increasing contribution of surface reflected, upward irradiance, which progressively dominates ΔF_{sol} of the cirrus. ΔF_{sol} is essentially a measure of the contrast between α_{srf} and α_{cld}, with α_{cld} mostly dependent on r_{eff} and IWC. In case of a highly reflective surface ($\alpha_{\mathrm{srf}} \geq 0.6$; Fig. 9d) the predominant cooling in the solar spectrum turns into a warming effect for most of the combinations with ΔF_{sol} up to 15–20 W m^{-2}. Only ice clouds with r_{eff} < 10 μm and IWC $\approx$ 0.1 g m^{-3}, i.e., high $\tau > 3$, are still more reflective than the surface. Such combinations of r_{eff} < 10 μm and IWC $\approx$ 0.1 g m^{-3} are associated with ice crystal number concentrations that are rarely observed in nature except for some cases of contrails (see Fig. 1 in Krämer et al. (2016)).

For cirrus over non-reflective or slightly reflective surfaces ($\alpha_{\mathrm{srf}} \leq 0.33$) and the Sun at intermediate SZA ($\theta \geq 30°$), the contour lines separate and the sensitivity of ΔF_{sol} on r_{eff} and IWC is reduced. For sun positions closest to the horizon ($\theta = 70°$) and above highly reflective surfaces ($\alpha_{\mathrm{srf}} = 1$), ΔF_{sol} is characterized by a generally low sensitivity over the entire range of IWC and r_{eff} (Fig. 9p). In spite of the warming effect for $\alpha_{\mathrm{srf}} = 1$ and $\theta \leq 30°$, the slant path of the incident radiation through the cloud reduces the surface influence and leads to a cooling effect with ΔF_{sol} in the range of -5 to -80 W m^{-2}.

3.4.2 Thermal-infrared

The TIR component of ΔF is insensitive to changes in θ and α_{srf}, and only combinations of IWC and r_{eff} are of relevance. In the TIR, the surface is approximated by a blackbody with a wavelength independent emissivity equal to one. The resulting distributions of ΔF_{net}, shown in Fig. 10, are dominated by the contribution of ΔF_{sol} and, therefore, are characterized by similar sensitivities. The strongest gradient of ΔF_{net} on IWC and r_{eff} are found for $\theta \approx 0°$ and $\alpha_{\mathrm{srf}} = 0$ (Fig. 10a). With increasing α_{srf}, ΔF_{net} is positive for the majority of the combinations of IWC and r_{eff} (Fig. 10c). The net warming is most pronounced for $\alpha_{\mathrm{srf}} = 1$ (Fig. 10d). It is further noted that for $\alpha_{\mathrm{srf}} = 1$ and high Sun ($\theta \leq 40°$), ΔF_{net} is positive and almost exclusively sensitive to IWC. Conversely, regions that have a net cooling effect, i.e., at high N_{ice} values, are exclusively sensitive to r_{eff}. The cloud can have a net cooling effect, when the Sun is close to horizon (Fig. 10p).

3.5 Sensitivity surface temperature and ice cloud altitude

Any variations in the surface temperature T_{srf} or ice cloud temperature T_{ice} (with associated cloud altitude z) leave ΔF_{sol} unaffected (Fig. 11a and Fig. 12a). Negligible differences in the medians of ± 2 W m^{-2} are due to the variation in the humidity profile. Increasing T_{srf} and therefore the temperature difference between surface and cirrus leads to an intensification of the TIR heating effect (see Eq. 14). The median is shifted from 1.2 to 4.5 W m^{-2} (Fig. 11b). Simultaneously, the distributions broaden with $Q_{\Delta \mathrm{F,tir}}$ ranging from 1.9 to 6.8 W m^{-2}, which results from the warmer and moister tropical profile used in

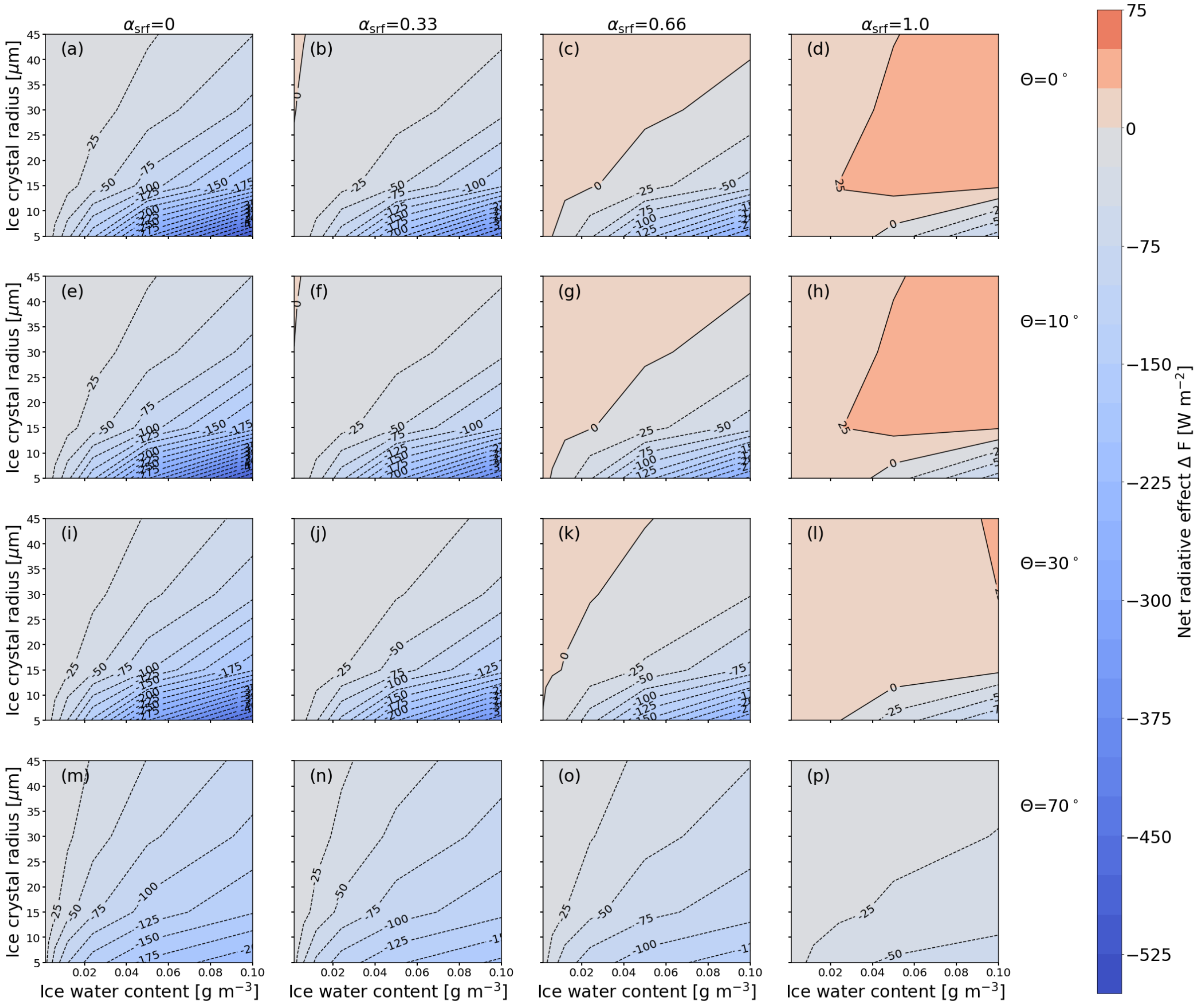

Figure 10. Same as Fig. 9 but for ΔF_{net}.

combination with $T_{\mathrm{srf}} = 313$ K compared to the dryer Arctic profile. As a result of constant ΔF_{sol} and the increase in ΔF_{tir}, the net heating effect is enhanced with medians ranging between 0.5 and 3.4 W m^{-2}.

A similar effect is found for the variation in T_{ice} that is presented in Fig. 12. With decreasing T_{ice} (increase in cloud base altitude), the temperature difference between T_{ice} and T_{srf} is increased, and reinforces the TIR heating effect. The median ΔF_{tir} increases from 5.3 to 11.9 W m^{-2} and for ΔF_{net} from 0.2 to 2.1 W m^{-2}. Compared to the impact of T_{srf}, which was varied over a range of 80 K, shifting the cloud in the vertical has only a minor effect on ΔF_{tir} and ΔF_{net}, as the variation in T_{ice} spanned only 27 K.

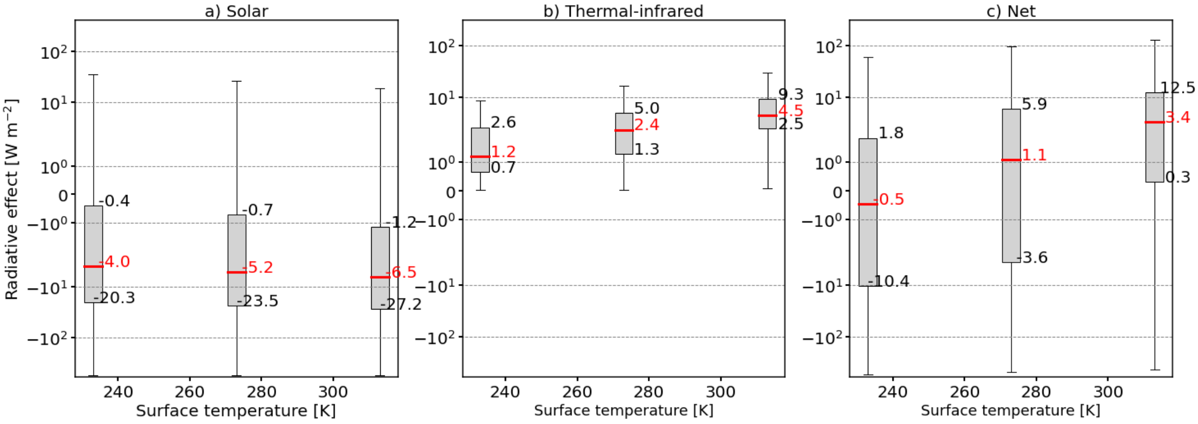

Figure 11. Same as Fig. 5 but for surface temperature T_{srf}.

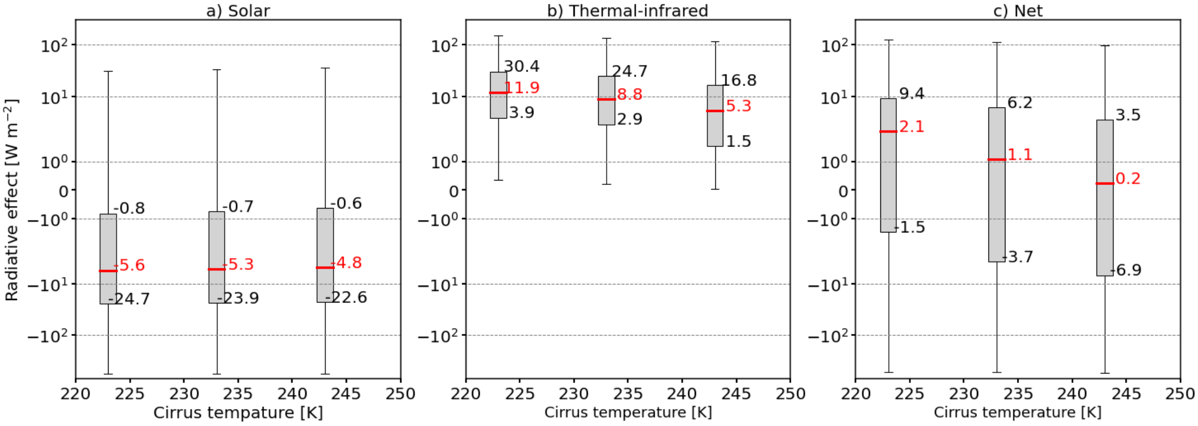

Figure 12. Same as Fig. 5 but for ice cloud temperature T_{ice}.

3.6 Sensitivity on underlying liquid water cloud

The impact of an additional liquid water cloud on the cirrus ΔF is presented in Fig. 13. A liquid water cloud optical thickness $\tau_{\mathrm{wc}} = 0$ is equivalent to the absence of secondary clouds and such conditions lead to the strongest ΔF_{sol} with a median of $-5.7\ \mathrm{W\,m^{-2}}$. By gradually increasing τ_{wc} the reflected, upward irradiance overlays and masks the impact of the surface. In general, the response of ΔF_{sol} on τ_{wc} is comparable to that of an increase in α_{srf}. Introducing a cloud with $\tau_{\mathrm{wc}} = 5$ slightly enhances the cooling in the solar spectrum ΔF_{sol} from -5.7 to $-6.5\ \mathrm{W\,m^{-2}}$. More relevant is the reduction in the variability of ΔF_{sol} with the distribution becoming narrower and reducing $Q_{\Delta \mathrm{F,sol}}$ from $-34.3\ \mathrm{W\,m^{-2}}$ to $25.2\ \mathrm{W\,m^{-2}}$. The smallest variance is found for $\tau_{\mathrm{wc}} = 20$ with $Q_{\Delta \mathrm{F,sol}} = -11.9\ \mathrm{W\,m^{-2}}$ and a median of $-2.9\ \mathrm{W\,m^{-2}}$ as the cloud almost entirely suppresses any contribution from the underlying surface.

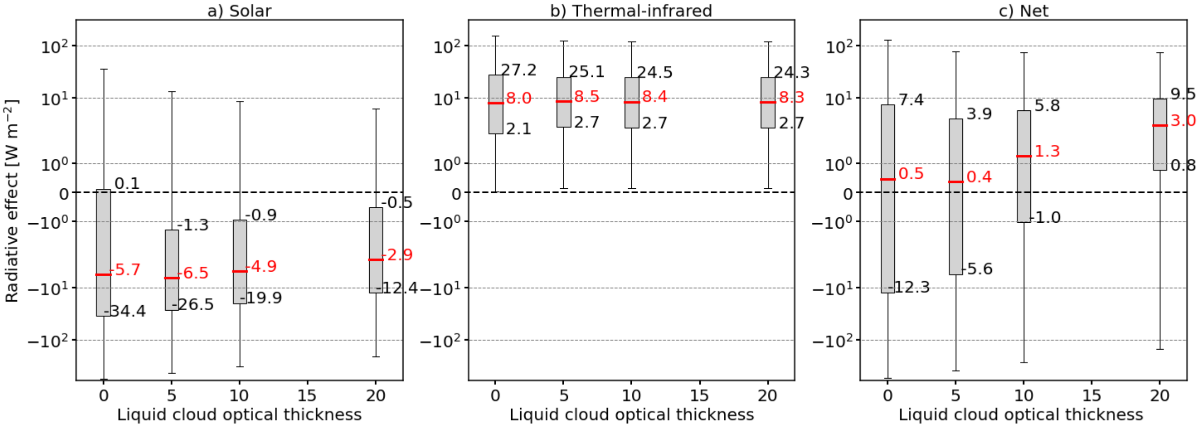

Figure 13. Same as Fig. 5 but for the underlying liquid water cloud optical thickness τ_{wc}.

An increase in τ_{wc} from 0 to 20 results in a minor response of ΔF_{tir}, shifting the median from 8 to 8.3 W m^{-2} and decreasing $Q_{\Delta \mathrm{F,tir}}$ at the same time. The reduction of maximum ΔF_{tir} is a consequence of the attenuated temperature difference ΔT between the liquid water cloud and the ice cloud compared to the surface. The effect on ΔF_{tir} is small as the change in temperature from surface to liquid water cloud is small. In case of the US standard atmosphere, where $\Delta T = 5$ K.

As a result of the reduced cooling in the solar spectrum, the net heating of the ice clouds intensifies. The median ΔF_{net} is shifted from 0.4 to 3.0 W m^{-2} with an accompanying decrease in the overall variance. While for $\tau_{\mathrm{wc}} < 5$ about 50 % of the combinations comprised a potential net cooling by the cirrus, positive ΔF_{net} is dominating for larger τ_{wc}.

Figure 14 shows ΔF_{sol} depending on IWC and r_{eff} separated for α_{srf} (columns) and τ_{wc} (rows). In the presented cases, a $\theta = 10°$ is selected as the influence of the surface and an additional cloud layer is of higher importance, when the Sun is close to the zenith. Due to the selection of θ, the top row in Fig. 14 is the same as the second row in Fig. 9 with similar characteristic features in distribution and sensitivity: largest RE appears over dark surfaces ($\alpha_{\mathrm{srf}} = 0$) in combination with clouds containing the largest ice number concentrations N_{ice} due to small r_{eff} and larger IWC. Over non-reflective surfaces, ΔF_{sol} is negative for all combinations and with increasing α_{srf} the warming in the solar range dominates (ΔF_{sol} up to 15 W m^{-2}; Fig. 14d). Introducing the second cloud layer and gradually increasing the τ_{wc} turns the previous solar warming to a cooling effect of around $\Delta F_{\mathrm{sol}} = -15$ W m^{-2} for the majority of the parameter combinations. Within those regions the second cloud layer also reduces the sensitivity on the ice cloud microphysical properties. Only cirrus with high N_{ice} can lead to a cooling of up to $\Delta F_{\mathrm{sol}} = -80$ W m^{-2}.

As shown in Fig. 13 the second cloud layer, at $z = 3$ km modifies ΔF_{tir} only slightly and multi-dimensional dependencies with respect to IWC, r_{eff}, α_{srf}, and τ_{wc} are weak leading to homogeneous distributions (not shown here). Figure 15 illustrates the variations in ΔF_{net}. For combinations of $\alpha_{\mathrm{srf}} \leq 0.66$ and $\tau_{\mathrm{ice}} \leq 5$, ΔF_{net} is determined by the solar component and its sensitivities. Special attention should be given to conditions with $\alpha_{\mathrm{srf}} > 0.66$ and $\tau_{\mathrm{ice}} > 5$, where ΔF_{net} turns from a cooling into a warming effect. This is due to the reduced ΔF_{sol} and the domination by ΔF_{tir}. In these situations ΔF_{net} ranges between

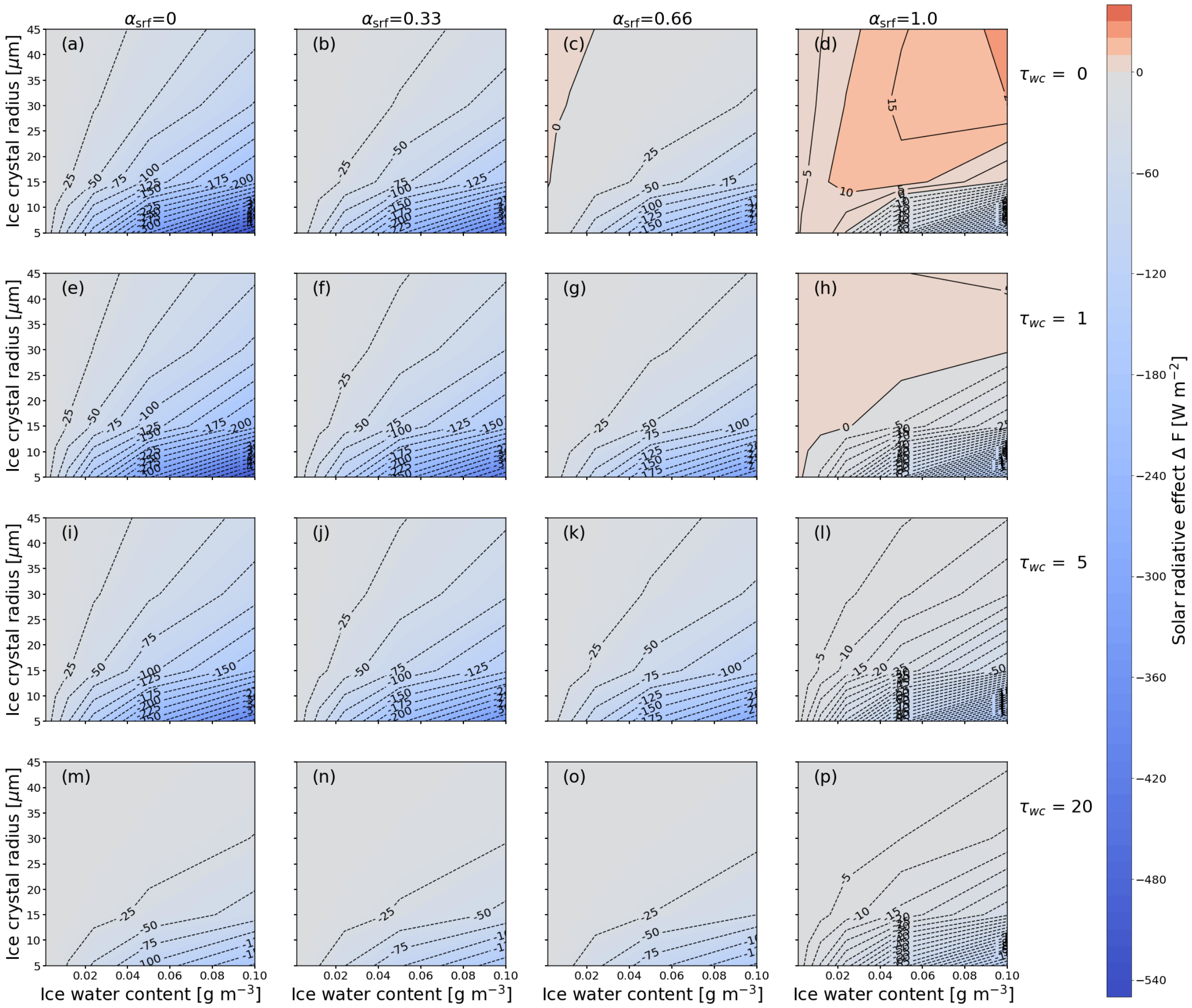

Figure 14. Same as Fig. 10 but ΔF_{sol} and combinations of surface albedo α_{srf} and cloud optical thickness τ_{liq} of the underlying liquid water cloud.

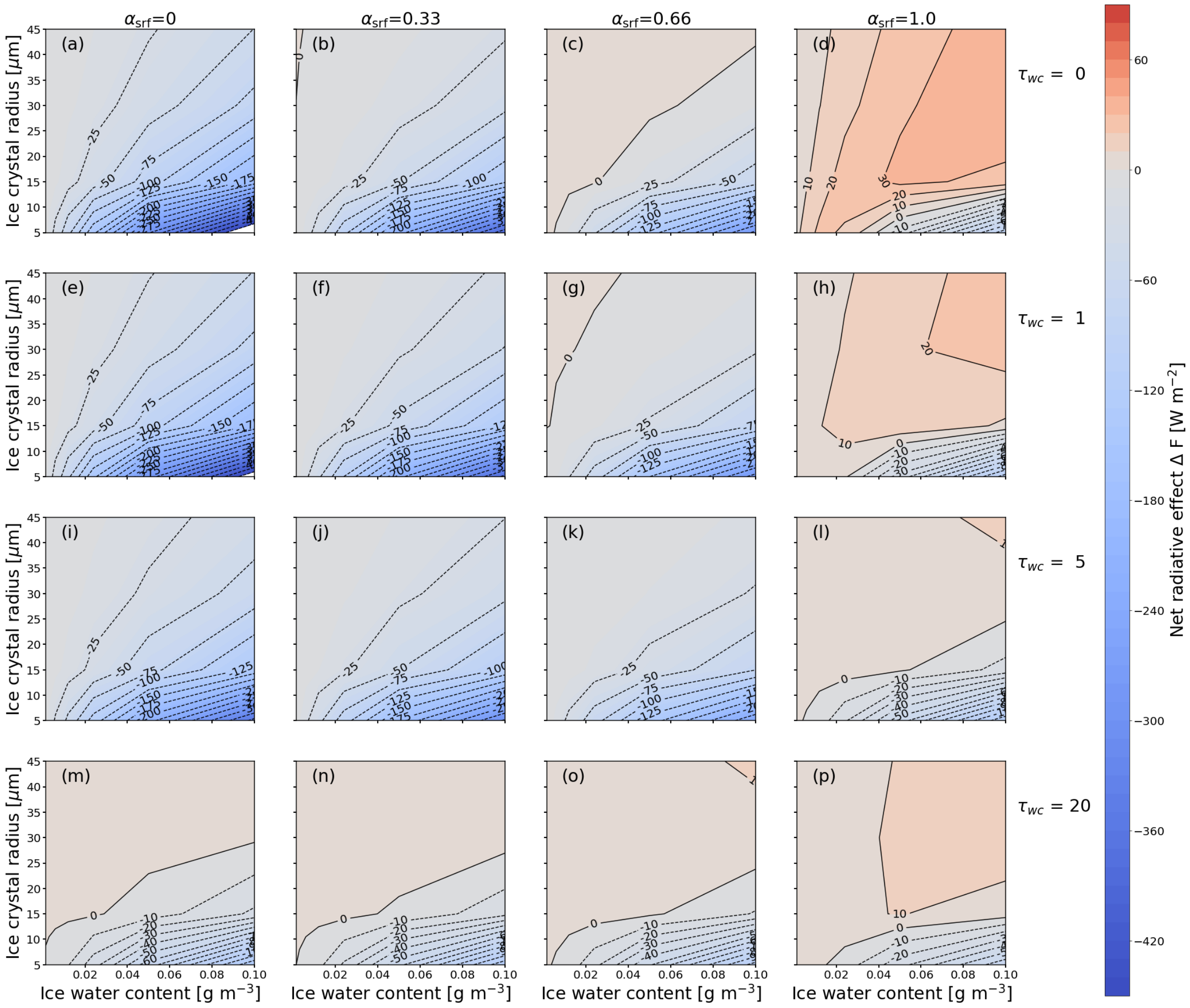

Figure 15. Same as Fig. 10 but for ΔF_{net} and combinations of surface albedo α_{srf} and cloud optical thickness τ_{liq} of the underlying liquid water cloud.

https://doi.org/10.5194/egusphere-2023-155
Preprint. Discussion started: 3 February 2023

0 and 20 W m^{-2} and is characterized by a low sensitivity with respect to r_{eff} and IWC of the ice cloud. An exception are clouds with extreme N_{ice}, where an increased cooling effect in relation to r_{eff} occurs.

4 Summary

The net RE of cirrus and contrails depends on multiple factors mainly the microphysical and macrophysical cloud properties, the related cloud optical properties, and radiative properties of the environment. The presented study aimed to separate the effect of eight selected parameters: solar zenith angle θ, ice water content IWC, ice crystal effective radius r_{eff}, cirrus temperature T_{ice}, surface albedo α_{srf}, surface temperature T_{srf}, liquid water cloud optical thickness τ_{liq} of an underlying cloud, and three ice crystal shapes on the cirrus RE. In total, 94,500 simulations have been performed that were constrained by their values and ranges that are typically associated with natural cirrus and contrails. Specific cases or sub-samples were selected and discussed, while the entire set of simulations is made available as a netCDF file that can be explored by the user (Wolf et al., 2023).

For the presented cases the cirrus RE was separated for the solar ΔF_{sol} and TIR ΔF_{tir} part of the spectrum, but also the combined net RE. Comparing to a chosen reference cloud with $\theta = 0°$, $T_{\text{ice}} = 223$ K, $\alpha_{\text{srf}} = 0$, $T_{\text{srf}} = 313$ K, IWC = 0.024 g m^{-3}, r_{eff} = 45 μm, τ_{wc} = 0 (no liquid water cloud), and resulting $\tau_{\text{ice}} = 0.18$ (at 640 nm) it was found that r_{eff} has the largest impact on solar, TIR, and net RE. The second most important parameter is the IWC, which impacts ΔF_{sol} and ΔF_{tir} equally. In the selected case, ΔF_{sol} and ΔF_{tir} have opposite signs, meaning that the IWC has a relatively small impact on ΔF_{net}. It has to be noted that the counter-balancing effect only appears during daytime, when $\Delta F_{\text{sol}} \neq 0$ W m^{-2}. At night, ΔF_{net} equals ΔF_{tir} and the cirrus heats the Earth-atmosphere-system. After r_{eff} and IWC, the solar RE of cirrus is determined by θ, α_{srf}, τ_{liq}, and the ice crystal shape in descending priority. The RE in the TIR spectrum is dominated by T_{srf}, T_{ice}, τ_{liq}, and the ice crystal shape. The combined net RE is controlled by α_{srf}, θ, and T_{srf} sorted in decreasing importance. The relevance of the input parameters can differ for other τ_{ice} and ambient condition.

The impact of individual input parameter on the solar, TIR, and net RE was further investigated by sub-sampling the entire set for one fixed parameter, while the remaining parameters can vary. This can be interpreted as a type of a sub-sampling, by averaging all unfixed values of RE, to project ΔF onto the one-dimensional space.

- For all θ and the majority of the simulations, ΔF_{sol} is dominated by ΔF_{tir} and leads to a positive median ΔF_{net} (warming).
- The projection of ΔF_{net} for varying α_{srf} showed that cirrus primarily cools in the solar, except for $\alpha_{\text{srf}} = 1$, e.g., over ice covered regions. Contrarily, ΔF_{tir} is positive and unaffected by the variations in α_{srf}. ΔF_{tir} determines the resulting ΔF_{net}, which leads to a net heating effect, when α_{srf} exceeds the critical range of 0.25–0.3.
- An increase in IWC intensifies the cooling in the solar and the heating in the TIR. As both effects compete against each other, the resulting net RE is a warming. An exception appears for largest IWC, where median ΔF_{net} is negative. Simultaneously, the increase in IWC causes an enhanced impact of the free parameters and associated uncertainties.

- Clouds with similar IWC but larger r_{eff} are comprised of fewer ice crystals, which reduces the clouds reflectivity. Over the entire range of r_{eff} the sub-sampled data set is characterized by a negative ΔF_{sol} that is most intense for the smallest crystals. Similarly, ΔF_{tir} is largest for small crystals and decreases for large crystals. While the solar and TIR ΔF become less intense with r_{eff}, the decrease is more pronounced for ΔF_{sol} such that cirrus primarily has a positive ΔF_{net}. An exception are clouds with the smallest r_{eff} and high IWC that occur only in contrails over non-reflective surfaces.
- The surface temperature T_{srf} and ice cloud temperature T_{ice} only affect the TIR component of ΔF. Decreasing T_{srf} or T_{ice} leads to an intensified TIR and net heating effect. Furthermore, T_{srf} and T_{ice} can be considered as belonging together in which TIR and net heating becomes larger with increasing difference among T_{srf} and T_{ice}.
- An underlying liquid water cloud with an increasing τ_{wc} leads to a reduction in solar ΔF_{sol}. Simultaneously, the TIR heating remains almost constant and the resulting ΔF_{net} increases with τ_{wc}.

It has to be noted that this study focused on the cloud RE of homogeneous, infinite ice cloud layers and neglected horizontal photon transport. The vertical and horizontal structure of ice clouds, i.e., distribution of ice water content, is typically heterogeneous, which is one reason for differences and uncertainties between 1D-simulated and the actual RE of such clouds (Fauchez et al., 2017, 2018). Additional differences originate from the IPA (Cahalan et al., 1994). Both effects have been primarily investigated for liquid water clouds, for example by Marshak and Davis (2005), while only few studies are available on cirrus 3D effects, e.g., Hogan and Kew (2005). Therefore, a follow-up study, that aims to determine and separate both effects, is currently ongoing.

Data availability. The three data-sets with all simulated irradiances, the calculated cloud radiative effect, and the ice cloud optical thickness are given in separate netCDF-files. Each file represents an individual ice crystal shape. The data is available on the zenodo platform via Wolf et al. (2023)

Appendix A: Overview over the multi-parameter dependencies

Figures A1 and A2 show solar ΔF_{sol} and TIR ΔF_{tir} (above diagonal), and net ΔF_{net} (below diagonal) for combinations of parameters indicated along the x- and y-axis. Both plots are intended to provide an overview over the multi-parameter dependencies. Within each sub-panel ΔF is given as a function of the x- and y-axis, while the other parameters are set to constant values that are representative of contrails and cirrus clouds. For example, the 'IWC–SZA' panel shows ΔF as a function of IWC, with $\theta = 30°$, T_{ice} = 233 K, $r_{\mathrm{eff}} = 15$ μm, $\alpha = 0.15$, $T_{\mathrm{srf}} = 273$ K, and without a second liquid water cloud ($\tau_{\mathrm{wc}} = 0$). This can be understood as a 2D–cross-section of the 8D hypercube. The black arrows indicate the gradient of the field. The gradient is computed with second order central differences and one-side differences at the boundaries of the field. The length of the arrow is only representative for an individual field and cannot be compared with the other fields as it depends

https://doi.org/10.5194/egusphere-2023-155
Preprint. Discussion started: 3 February 2023

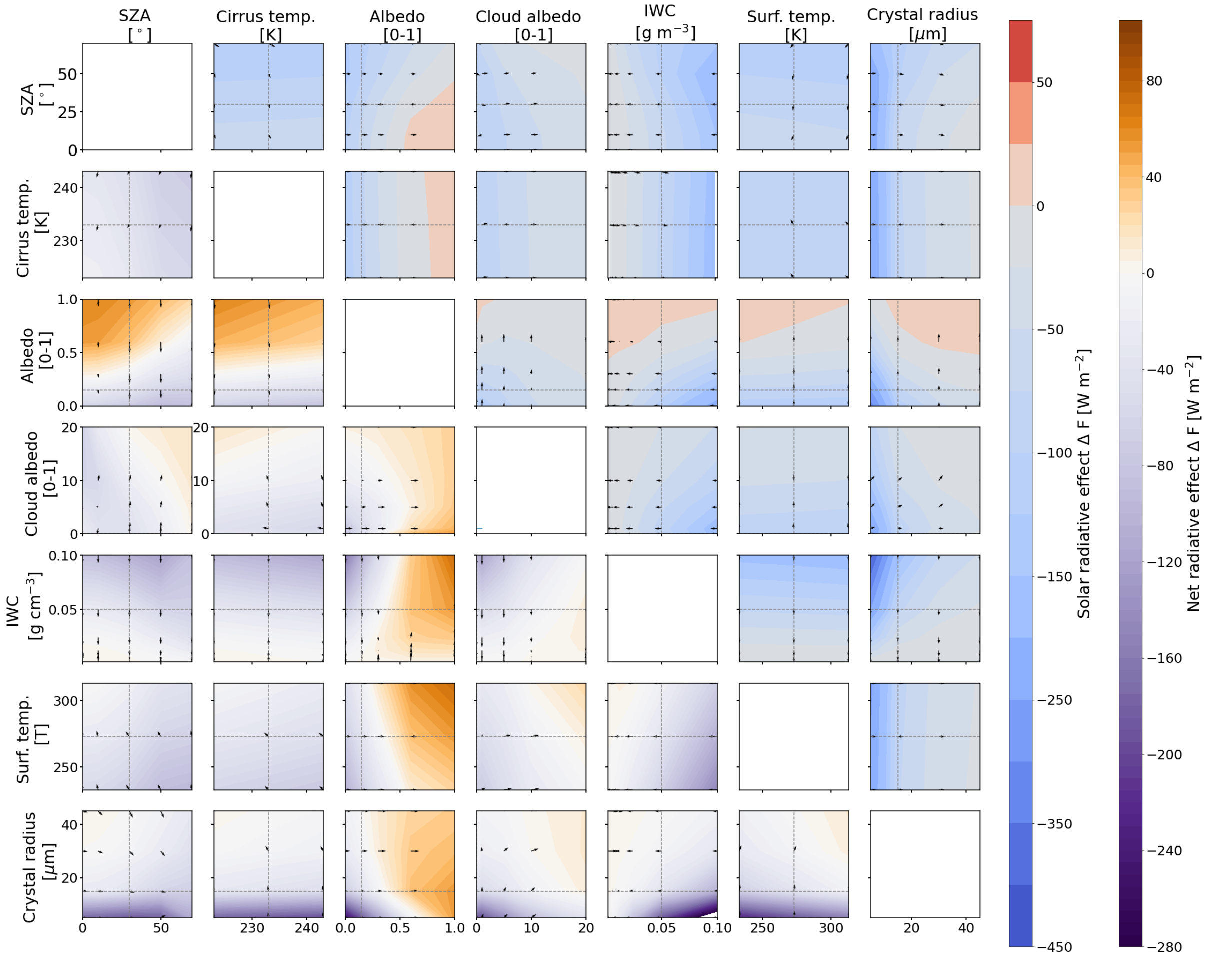

Figure A1. Above diagonal panels: Plot of median solar ΔF_{sol} projected in two-dimensional parameter space. Blue colors indicate negative ΔF_{sol} (cooling), while red colors indicate positive ΔF_{sol} (warming). Below diagonal panels: Same as above diagonal but for median net ΔF_{net}. Purple shades indicate negative ΔF_{net} (cooling), while orange shades indicate positive ΔF_{net} (warming). The black arrows point to the direction of the steepest slope.

on the units of the parameters. Therefore, the arrows are normalized and can only be interpreted for their direction and not for their length.

Appendix B: Simulation time and accuracy

550 The radiative transfer solver fdisort2 (Stamnes et al., 2000) allows to select $2N$-number of streams to be used in the radiative transfer simulations. Higher number of streams increases the accuracy of the simulations but also the computational time. To obtain sufficient accuracy while keeping the computational time reasonable, the optimal trade-off was estimated by progres-

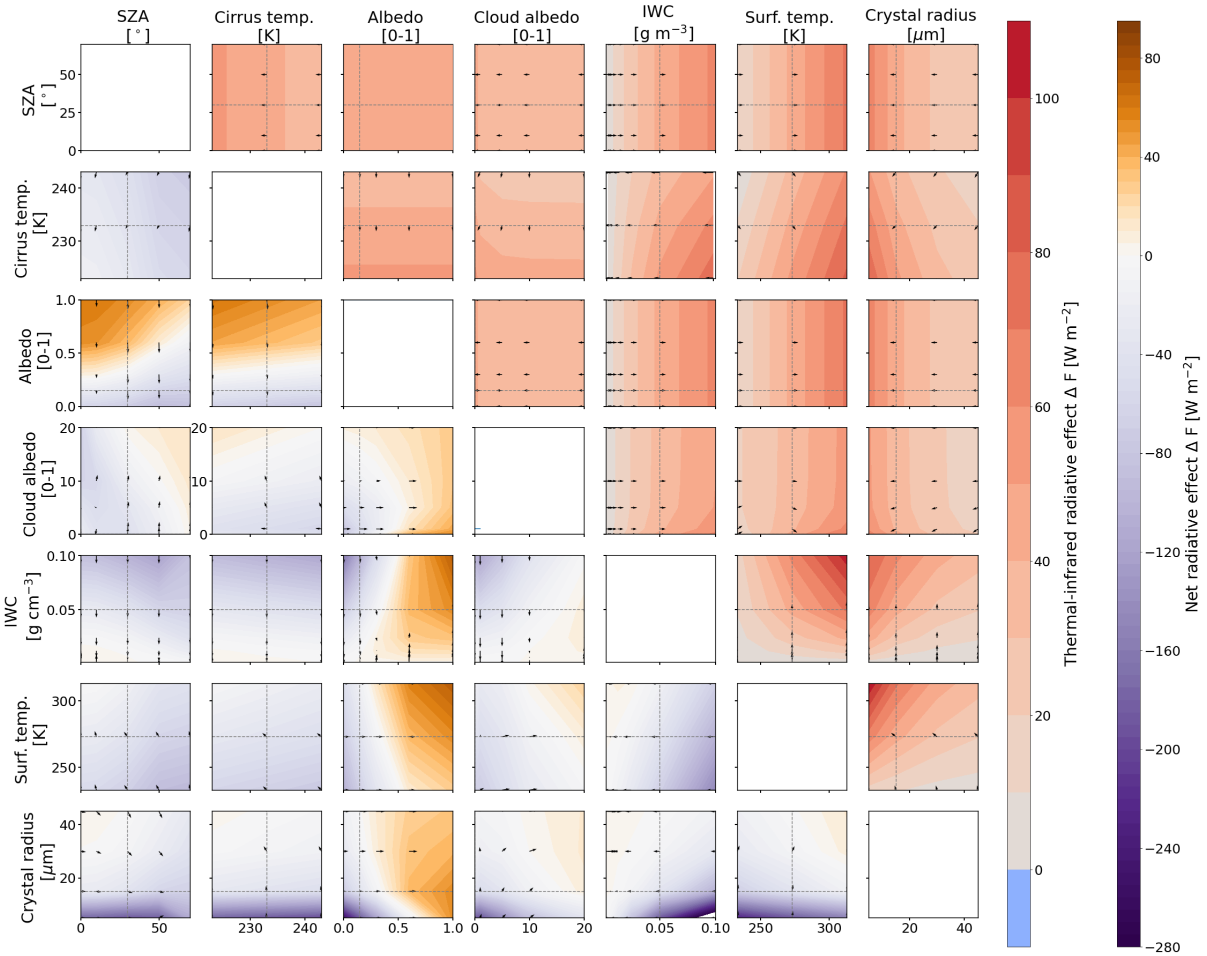

Figure A2. Same as Fig. A1 but above diagonal panels present median TIR ΔF_{tir}.

sively increasing the number of streams from 4 to 48. The simulation with 48 streams is regarded as the reference with the highest accuracy and computational time.

555 The number of streams and the timing of the RT simulations is estimated on basis of a specific parameter combination, representing a complex cloud scene that is characterized by cloud–cloud–surface-interactions. The simulations are run for a solar zenith angle $\theta = 70°$, a cirrus temperature T_{ice} of 233 K, a surface albedo $\alpha_{\mathrm{srf}} = 1$, an ice water content $IWC = 2.4 \cdot 10^{-3}\,\mathrm{g\,m^{-3}}$, a surface temperature $T_{\mathrm{srf}} = 270$ K, an ice crystal effective radius $r_{\mathrm{eff}} = 5\,\mu\mathrm{m}$, and an additionally underlying liquid water cloud (cloud optical thickness τ_{liq} = 10).

560 The computational time that is required for the simulations depends on the available hardware. Therefore, we provide the fraction of time that is required and relate it to the maximum duration using 48 streams. The accuracy is given as the relative difference between the cloud RE for a given number of streams with respect to the reference simulation.

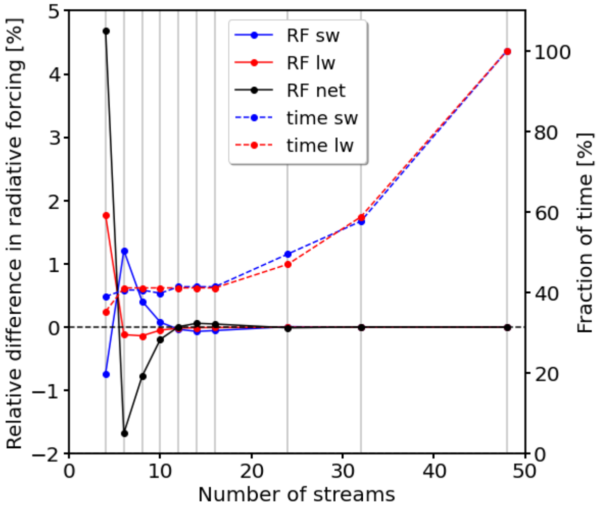

Figure B1. Relative deviation (in %) of solar (blue), TIR (red), and net (black) cloud radiative effect from the reference simulation calculated with 48 streams. The computational time is given as the fraction of the maximum duration needed for solar (blue, dashed) or TIR (red, dashed) simulations using the maximum number of 48 streams.

Figure B1 shows that the relative difference in the RE decreases with increasing number of streams (higher accuracy). A significant gain in accuracy is achieved by switching from 4 to 10 streams. For simulations with 12 to 16 streams the relative difference remains constant at around 0.1 %. Further increasing to 24 streams provides only slight gain in accuracy, whereas the computational time increases disproportionaly. Therefore, the simulations in this study were run with 16 streams as it provides the optimal trade-off between accuracy and computational time.

Appendix C: Single-scattering phase function $\mathcal{P}$

The selected ice crystal shape is an important factor in RT simulations. Kahnert et al. (2008) found that the shape-effect on the cloud RE is up to 20 $\mathrm{W\,m^{-2}}$, which is, in their study, equivalent to a change in surface albedo α_{srf} from 0.4 to 0.8 or altering the ice water content IWC of the cloud by a factor of 2. The shape-effect is primarily caused by differences in the extinction of radiation and the asymmetry parameter, which itself depends on the scattering phase function $\mathcal{P}$ (Kahnert et al., 2008). $\mathcal{P}$ provides the angular distribution of the scattered direction in relation to the incident light. As an example, Fig. C1a–d shows $\mathcal{P}$ at 550 nm wavelength for columns, plates, droxtals, and a mixture of aggregated crystals (hollow column; bullets; rosettes), respectively. The phase functions are extracted from the post-processed libRadtran data set that is based on the ice optics computations from Yang et al. (2000).

All ice crystal shapes are characterized by a dominating peak in the forward direction, which drops by a factor of 10^4 sr^{-1}, when the scattering angle Θ increases from 0° to 10°. For $10° < \Theta < 160°$, $\mathcal{P}$ remains mostly flat with values between 10^{-1} sr^{-1} and 10^{1} sr^{-1}. Towards $\Theta > 160°$ the phase function increases, showing enhanced backward scattering except for the

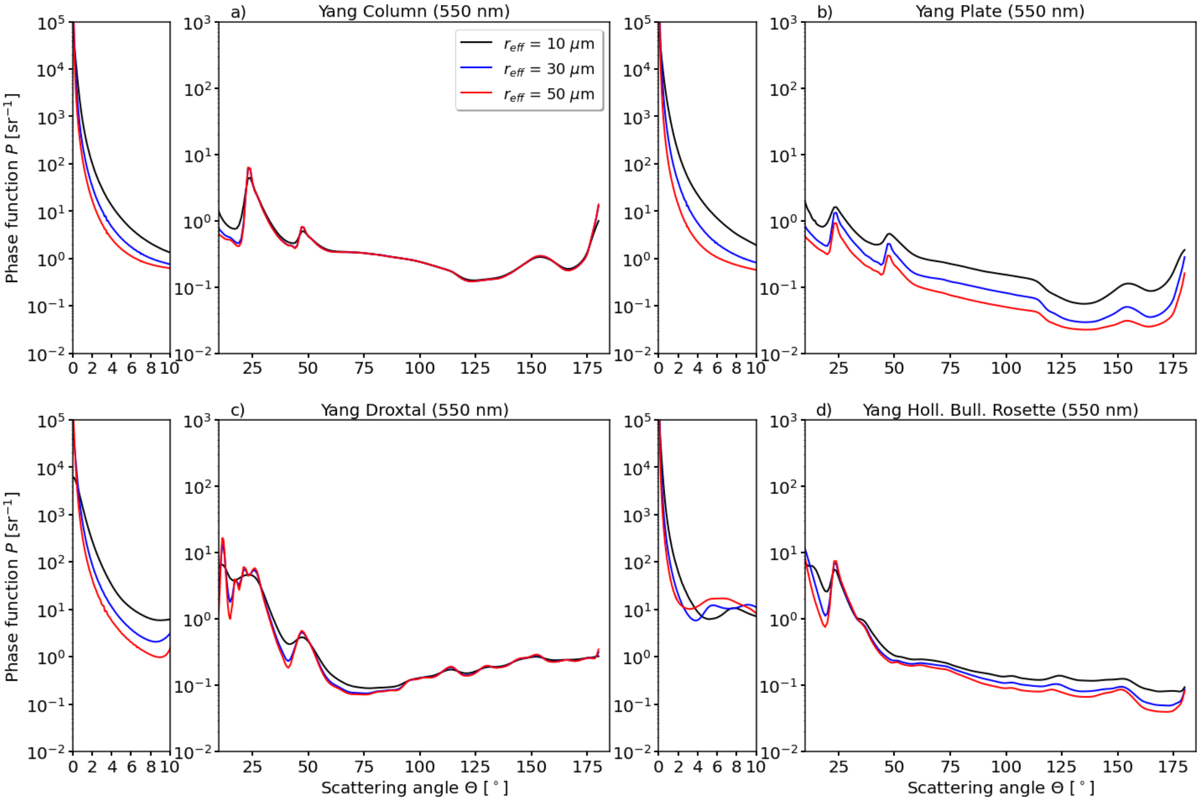

Figure C1. Phase function of four different ice crystal habits and three particle size distributions at 550 nm. Plot of the (1,1)-element of the scattering phase matrix. Two different y-scales are applied depending on the size of the forward scattering peak. Plotted $\mathcal{P}$ are post-processed phase functions from Emde et al. (2016) that are based on Yang et al. (2000). The phase functions from Emde et al. (2016) assume a size distribution that follows a gamma function.

580 complex shaped crystals (Fig. C1d). Further characteristics of $\mathcal{P}$ are local maxima at 22° and 46° scattering angles that appear for columns, plates, and droxtals (Fig. C1a–c), and cause halo phenomena. For the crystal mixture and aggregated crystals (Fig. C1d) the second peak is barely noticeable as the surface roughness and shape complexity smooths angular-dependent scattering in $\mathcal{P}$. Additionally, non-spherical crystals (Fig. C1a,b,d) have enhanced sideward scattering compared to ice crystals with a roughly spherical shape, like droxtals (Fig. C1c) or water droplets. Another characteristic is the shift in the $\mathcal{P}$ from
585 variations in the crystal radius r_{eff}, which is most prominent for plates and lowest for columns.

Author contributions. **KW** designed the model setup, conducted the experiments and the data analysis, and prepared the manuscript. **NB** and **OB** contributed equally to the preparation of the manuscript.

Competing interests. The authors declare no competing interest.

Acknowledgements. The authors acknowledge support from the Direction Générale de l'Aviation Civile through the Convention N°2021-39 relative to "Aviation & Climate".

References

Anderson, G., Clough, S., Kneizys, F., Chetwynd, J., and Shettle, E.: AFGL Atmospheric Constituent Profiles (0.120km), p. 46, 1986.

Baldridge, A. M., Hook, S. J., Grove, C. I., and Rivera, G.: The ASTER spectral library version 2.0, Remote Sens. Environ., 113, 711–715, https://doi.org/10.1016/j.rse.2008.11.007, 2009.

Bauer, P., Thorpe, A., and Brunet, G.: The quiet revolution of numerical weather prediction., Nature, 525, 47–55, https://doi.org/10.1038/nature14956, 2015.

Baum, B. A., Yang, P., Heymsfield, A. J., Platnick, S., King, M. D., Hu, Y.-X., and Bedka, S. T.: Bulk scattering properties for the remote sensing of ice clouds. Part II: narrowband models, J. Appl. Meteorol., 44, 1896 – 1911, https://doi.org/10.1175/JAM2309.1, 2005.

Baum, B. A., Yang, P., Nasiri, S., Heidinger, A. K., Heymsfield, A., and Li, J.: Bulk scattering properties for the remote sensing of ice clouds. Part III: high-resolution spectral models from 100 to 3250 cm-1, J. Appl. Meteorol., 46, 423 – 434, https://doi.org/10.1175/JAM2473.1, 2007.

Bi, L., Yang, P., Liu, C., Yi, B., Baum, B. A., van Diedenhoven, B., and Iwabuchi, H.: Assessment of the accuracy of the conventional ray-tracing technique: Implications in remote sensing and radiative transfer involving ice clouds, J. Quant. Spectrosc. Radiat. Transfer, 146, 158–174, https://doi.org/10.1016/j.jqsrt.2014.03.017, 2014.

Bickel, M., Ponater, M., Bock, L., Burkhardt, U., and Reineke, S.: Estimating the Effective Radiative Forcing of Contrail Cirrus, J. Climate, 33, 1991 – 2005, https://doi.org/10.1175/JCLI-D-19-0467.1, 2020.

Bräuer, T., Voigt, C., Sauer, D., Kaufmann, S., Hahn, V., Scheibe, M., Schlager, H., Diskin, G. S., Nowak, J. B., DiGangi, J. P., Huber, F., Moore, R. H., and Anderson, B. E.: Airborne measurements of contrail ice properties–dependence on temperature and humidity, Geophys. Res. Lett., 48, e2020GL092 166, https://doi.org/10.1029/2020GL092166, 2021.

Burkhardt, U. and Kärcher, B.: Global radiative forcing from contrail cirrus, Nat. Clim. Change, 1, 54–58, https://doi.org/10.1038/nclimate1068, 2011.

Cahalan, R. F., Ridgway, W., Wiscombe, W. J., Bell, T. L., and Snider, J. B.: The albedo of fractal stratocumulus clouds, J. Atmos. Sci., 51, 2434 – 2455, https://doi.org/10.1175/1520-0469(1994)051<2434:TAOFSC>2.0.CO;2, 1994.

Campbell, J. R., Lolli, S., Lewis, J. R., Gu, Y., and Welton, E. J.: Daytime cirrus cloud top-of-the-atmosphere radiative forcing properties at a midlatitude site and their global consequences, J. Appl. Meteorology and Climatology, 55, 1667 – 1679, https://doi.org/10.1175/JAMC-D-15-0217.1, 2016.

Chen, T., Rossow, W. B., and Zhang, Y.: Radiative effects of cloud-type variations, J. Climate, 13, 264 – 286, https://doi.org/10.1175/1520-0442(2000)013<0264:REOCTV>2.0.CO;2, 2000.

Deirmendjian, D.: Scattering and polarization properties of polydispersed suspensions with partial absorption, Tech. rep., RAND CORP SANTA MONICA CA, 1962.

Emde, C., Buras-Schnell, R., Kylling, A., Mayer, B., Gasteiger, J., Hamann, U., Kylling, J., Richter, B., Pause, C., Dowling, T., and Bugliaro, L.: The libRadtran software package for radiative transfer calculations (version 2.0.1), Geosci. Model Dev., 9, 1647–1672, https://doi.org/10.5194/gmd-9-1647-2016, 2016.

Fauchez, T., Platnick, S., Meyer, K., Cornet, C., Szczap, F., and Várnai, T.: Scale dependence of cirrus horizontal heterogeneity effects on TOA measurements – Part I: MODIS brightness temperatures in the thermal infrared, Atmos. Chem. Phys., 17, 8489–8508, https://doi.org/10.5194/acp-17-8489-2017, 2017.

Fauchez, T., Platnick, S., Várnai, T., Meyer, K., Cornet, C., and Szczap, F.: Scale dependence of cirrus heterogeneity effects. Part II: MODIS NIR and SWIR channels, Atmos. Chem. Phys., 18, 12 105–12 121, https://doi.org/10.5194/acp-18-12105-2018, 2018.

Freudenthaler, V., Homburg, F., and Jäger, H.: Optical parameters of contrails from lidar measurements: Linear depolarization, Geophys. Res. Lett., 23, 3715–3718, https://doi.org/10.1029/96GL03646, 1996.

Fu, Q.: An accurate parameterization of the solar radiative properties of cirrus clouds for climate models, J. Climate, 9, 2058–2082, https://doi.org/10.1175/1520-0442(1998)011<2223:AAPOTI>2.0.CO;2, 1996.

Fu, Q. and Liou, K. N.: On the correlated k-distribution method for radiative transfer in nonhomogeneous atmospheres, J. Atmos. Sci., 49, 2139 – 2156, https://doi.org/10.1175/1520-0469(1992)049<2139:OTCDMF>2.0.CO;2, 1992.

Fu, Q. and Liou, K. N.: Parameterization of the radiative properties of cirrus clouds, J. Atmos. Sci., 50, 2008 – 2025, https://doi.org/10.1175/1520-0469(1993)050<2008:POTRPO>2.0.CO;2, 1993.

Gardner, A. S. and Sharp, M. J.: A review of snow and ice albedo and the development of a new physically based broadband albedo parameterization, J. Geophys. Res. Earth Surf., 115, F01 009, https://doi.org/10.1029/2009JF001444, 2010.

Gasteiger, J., Emde, C., Mayer, B., Buras, R., Buehler, S., and Lemke, O.: Representative wavelengths absorption parameterization applied to satellite channels and spectral bands, J. Quant. Spectrosc. Radiat. Transfer, 148, 99–115, https://doi.org/10.1016/j.jqsrt.2014.06.024, 2014.

Gayet, J.-F., Shcherbakov, V., Voigt, C., Schumann, U., Schäuble, D., Jessberger, P., Petzold, A., Minikin, A., Schlager, H., Dubovik, O., and Lapyonok, T.: The evolution of microphysical and optical properties of an A380 contrail in the vortex phase, Atmos. Chem. Phys., 12, 6629–6643, https://doi.org/10.5194/acp-12-6629-2012, 2012.

Goodman, J., Pueschel, R. F., Jensen, E. J., Verma, S., Ferry, G. V., Howard, S. D., Kinne, S. A., and Baumgardner, D.: Shape and size of contrails ice particles, Geophys. Res. Lett., 25, 1327–1330, https://doi.org/10.1029/97GL03091, 1998.

Gueymard, C. A., Lara-Fanego, V., Sengupta, M., and Xie, Y.: Surface albedo and reflectance: Review of definitions, angular and spectral effects, and intercomparison of major data sources in support of advanced solar irradiance modeling over the Americas, Sol. Energy, 182, 194–212, https://doi.org/10.1016/j.solener.2019.02.040, 2019.

Hansen, J. E. and Travis, L. D.: Light scattering in planetary atmospheres, Space Sci. Rev., 16, 527–610, https://doi.org/10.1007/BF00168069, 1974.

Haywood, J. M., Allan, R. P., Bornemann, J., Forster, P. M., Francis, P. N., Milton, S., Rädel, G., Rap, A., Shine, K. P., and Thorpe, R.: A case study of the radiative forcing of persistent contrails evolving into contrail-induced cirrus, J. Geophys. Res. Atmos., 114, D24 201, https://doi.org/10.1029/2009JD012650, 2009.

Hogan, R. J. and Kew, S. F.: A 3D stochastic cloud model for investigating the radiative properties of inhomogeneous cirrus clouds, Quarterly Journal of the Royal Meteorological Society, 131, 2585–2608, https://doi.org/10.1256/qj.04.144, 2005.

Jensen, E. J., Kinne, S., and Toon, O. B.: Tropical cirrus cloud radiative forcing: Sensitivity studies, Geophys. Res. Let., 21, 2023–2026, https://doi.org/10.1029/94GL01358, 1994.

Jeßberger, P., Voigt, C., Schumann, U., Sölch, I., Schlager, H., Kaufmann, S., Petzold, A., Schäuble, D., and Gayet, J.-F.: Aircraft type influence on contrail properties, Atmos. Chem. Phys., 13, 11 965–11 984, https://doi.org/10.5194/acp-13-11965-2013, 2013.

Kahnert, M., Sandvik, A. D., Biryulina, M., Stamnes, J. J., and Stamnes, K.: Impact of ice particle shape on short-wave radiative forcing: A case study for an arctic ice cloud, J. Quant. Spectrosc. Radiat. Transfer, 109, 1196–1218, https://doi.org/10.1016/j.jqsrt.2007.10.016, 2008.

Key, J. R., Yang, P., Baum, B. A., and Nasiri, S. L.: Parameterization of shortwave ice cloud optical properties for various particle habits, J. Geophys. Res. Atmos., 107, AAC 7–1–AAC 7–10, https://doi.org/https://doi.org/10.1029/2001JD000742, 2002.

Krämer, M., Rolf, C., Luebke, A., Afchine, A., Spelten, N., Costa, A., Meyer, J., Zöger, M., Smith, J., Herman, R. L., Buchholz, B., Ebert, V., Baumgardner, D., Borrmann, S., Klingebiel, M., and Avallone, L.: A microphysics guide to cirrus clouds – Part 1: Cirrus types, Atmos. Chem. Phys., 16, 3463–3483, https://doi.org/10.5194/acp-16-3463-2016, 2016.

Krämer, M., Rolf, C., Spelten, N., Afchine, A., Fahey, D., Jensen, E., Khaykin, S., Kuhn, T., Lawson, P., Lykov, A., Pan, L. L., Riese, M., Rollins, A., Stroh, F., Thornberry, T., Wolf, V., Woods, S., Spichtinger, P., Quaas, J., and Sourdeval, O.: A microphysics guide to cirrus – Part 2: Climatologies of clouds and humidity from observations, Atmos. Chem. Phys., 20, 12 569–12 608, https://doi.org/10.5194/acp-20-12569-2020, 2020.

Kurucz, R. L.: Synthetic infrared spectra, Infrared solar physics: proceedings of the 154th Symposium of the International Astronomical Union, 1992.

Lawson, R. P., Heymsfield, A. J., Aulenbach, S. M., and Jensen, T. L.: Shapes, sizes and light scattering properties of ice crystals in cirrus and a persistent contrail during SUCCESS, Geophys. Res. Lett., 25, 1331–1334, https://doi.org/10.1029/98GL00241, 1998.

Lee, D. S., Fahey, D. W., Skowron, A., Allen, M. R., Burkhardt, U., Chen, Q., Doherty, S. J., Freeman, S., Forster, P. M., Fuglestvedt, J., Gettelman, A., De León, R. R., Lim, L. L., Lund, M. T., Millar, R. J., Owen, B., Penner, J. E., Pitari, G., Prather, M. J., Sausen, R., and Wilcox, L. J.: The contribution of global aviation to anthropogenic climate forcing for 2000 to 2018, Atmos. Environ., 244, 117 834, https://doi.org/10.1016/j.atmosenv.2020.117834, 2021.

Liou, K.-N.: Influence of cirrus clouds on weather and climate processes: A global perspective, Mon. Weather Rev., 114, 1167 – 1199, https://doi.org/10.1175/1520-0493(1986)114<1167:IOCCOW>2.0.CO;2, 1986.

Lohmann, U. and Roeckner, E.: Influence of cirrus cloud radiative forcing on climate and climate sensitivity in a general circulation model, J. Geophys. Res. Atmos., 100, 16 305–16 323, https://doi.org/https://doi.org/10.1029/95JD01383, 1995.

Luebke, A. E., Afchine, A., Costa, A., Grooß, J.-U., Meyer, J., Rolf, C., Spelten, N., Avallone, L. M., Baumgardner, D., and Krämer, M.: The origin of midlatitude ice clouds and the resulting influence on their microphysical properties, Atmos. Chem. Phys., 16, 5793–5809, https://doi.org/10.5194/acp-16-5793-2016, 2016.

Luebke, A. E., Ehrlich, A., Schäfer, M., Wolf, K., and Wendisch, M.: An assessment of macrophysical and microphysical cloud properties driving radiative forcing of shallow trade-wind clouds, Atmos. Chem. Phys., 22, 2727–2744, https://doi.org/10.5194/acp-22-2727-2022, 2022.

Macke, A. and Großklaus, M.: Light scattering by nonspherical raindrops: Implications for lidar remote sensing of rainrates, J. Quant. Spectrosc. Radiat. Transfer, 60, 355–363, https://doi.org/10.1016/S0022-4073(98)00011-9, 1998.

Macke, A., Mishchenko, M. I., and Cairns, B.: The influence of inclusions on light scattering by large ice particles, J. Geophys. Res. Atmos., 101, 23 311–23 316, https://doi.org/10.1029/96JD02364, 1996a.

Macke, A., Mueller, J., and Raschke, E.: Single scattering properties of atmospheric ice crystals, J. Atmos. Sci., 53, 2813 – 2825, https://doi.org/10.1175/1520-0469(1996)053<2813:SSPOAI>2.0.CO;2, 1996b.

Macke, A., Francis, P. N., McFarquhar, G. M., and Kinne, S.: The role of ice particle shapes and size distributions in the single scattering properties of cirrus clouds, J. Atmos. Sci., 55, 2874 – 2883, https://doi.org/10.1175/1520-0469(1998)055<2874:TROIPS>2.0.CO;2, 1998.

Marshak, A. and Davis, A., eds.: 3D radiative transfer in cloudy atmospheres, Springer Berlin, Heidelberg, 1 edn., https://doi.org/10.1007/3-540-28519-9, 2005.

Meerdink, S. K., Hook, S. J., Roberts, D. A., and Abbott, E. A.: The ECOSTRESS spectral library version 1.0, Remote Sens. Environ., 230, 111 196, https://doi.org/10.1016/j.rse.2019.05.015, 2019.

Meerkötter, R., Schumann, U., Doelling, D. R., Minnis, P., Nakajima, T., and Tsushima, Y.: Radiative forcing by contrails, Ann. Geophys., 17, 1080–1094, https://doi.org/10.1007/s00585-999-1080-7, 1999.

Mie, G.: Beiträge zur Optik trüber Medien, speziell kolloidaler Metallösungen, Ann. Phys., 330, 377–445, https://doi.org/10.1002/andp.19083300302, 1908.

Mishchenko, M. I.: Comprehensive thematic T-matrix reference database: a 2017–2019 update, J. Quant. Spectrosc. Radiat. Transfer, 242, 106 692, https://doi.org/10.1016/j.jqsrt.2019.106692, 2020.

Mitchell, D. L., Lawson, R. P., and Baker, B.: Understanding effective diameter and its application to terrestrial radiation in ice clouds, Atmos. Chem. Phys., 11, 3417–3429, https://doi.org/10.5194/acp-11-3417-2011, 2011.

Nazaryan, H., McCormick, M. P., and Menzel, W. P.: Global characterization of cirrus clouds using CALIPSO data, J. Geophys. Res. Atmos., 113, D16 211, https://doi.org/10.1029/2007JD009481, 2008.

Petty, G. W. and Huang, W.: The modified gamma size distribution applied to inhomogeneous and nonspherical particles: Key relationships and conversions, J. Atmos. Sci., 68, 1460 – 1473, https://doi.org/10.1175/2011JAS3645.1, 2011.

Petzold, A., Busen, R., Schröder, F. P., Baumann, R., Kuhn, M., Ström, J., Hagen, D. E., Whitefield, P. D., Baumgardner, D., Arnold, F., Borrmann, S., and Schumann, U.: Near-field measurements on contrail properties from fuels with different sulfur content, J. Geophys. Res. Atmos., 102, 29 867–29 880, https://doi.org/10.1029/97JD02209, 1997.

Quaas, J., Gryspeerdt, E., Vautard, R., and Boucher, O.: Climate impact of aircraft-induced cirrus assessed from satellite observations before and during COVID-19, Environ. Res. Let., 16, 064 051, https://doi.org/10.1088/1748-9326/abf686, 2021.

Ramanathan, V., Cess, R. D., Harrison, E. F., Minnis, P., Barkstrom, B. R., Ahmad, E., and Hartmann, D.: Cloud-radiative forcing and climate: Results from the Earth radiation budget experiment, Science, 243, 57–63, http://www.jstor.org/stable/1703174, 1989.

Sassen, K.: Contrail-Cirrus and Their Potential for Regional Climate Change, Bull. Am. Meteorol. Soc., 78, 1885 – 1904, https://doi.org/10.1175/1520-0477(1997)078<1885:CCATPF>2.0.CO;2, 1997.

Sassen, K., Wang, Z., and Liu, D.: Global distribution of cirrus clouds from CloudSat/Cloud-Aerosol Lidar and Infrared Pathfinder Satellite Observations (CALIPSO) measurements, J. Geophys. Res. Atmos., 113, D00A12, https://doi.org/10.1029/2008JD009972, 2008.

Schröder, F., Kärcher, B., Duroure, C., Ström, J., Petzold, A., Gayet, J.-F., Strauss, B., Wendling, P., and Borrmann, S.: On the transition of contrails into cirrus clouds, J. Atmos. Sci., 57, 464 – 480, https://doi.org/10.1175/1520-0469(2000)057<0464:OTTOCI>2.0.CO;2, 2000.

Schumann, U.: On conditions for contrail formation from aircraft exhausts, Meteorologische Zeitschrift, 5, 1996.

Schumann, U.: Contrail Cirrus, in Cirrus, Oxford University Press, 1 edn., 2002.

Schumann, U.: A contrail cirrus prediction model, Geosci. Model Dev., 5, 543–580, https://doi.org/10.5194/gmd-5-543-2012, 2012.

Stamnes, K., Tsay, S.-C., Wiscombe, W., and Laszlo, I.: DISORT, a general-purpose Fortran program for discrete-ordinate-method radiative transfer in scattering and emittinglayered media: Documentation of methodology., Tech. rep., Stevens Institute of Technology Dept. of Physics and EngineeringPhysics Tech., 2000.

Stapf, J., Ehrlich, A., and Wendisch, M.: Influence of thermodynamic state changes on surface cloud radiative forcing in the Arctic: A comparison of two approaches using data from AFLUX and SHEBA, J. Geophys. Res. Atmos., 126, e2020JD033 589, https://doi.org/10.1029/2020JD033589, 2021.

Stephens, G. L.: Radiation profiles in extended water clouds. II: Parameterization schemes, J. Atmos. Sci., 35, 2123 – 2132, https://doi.org/10.1175/1520-0469(1978)035<2123:RPIEWC>2.0.CO;2, 1978.

Stephens, G. L., Tsay, S.-C., Stackhouse, P. W., and Flatau, P. J.: The relevance of the microphysical and radiative properties of cirrus clouds to climate and climatic feedback, J. Atmos. Sci., 47, 1742 – 1754, https://doi.org/10.1175/1520-0469(1990)047<1742:TROTMA>2.0.CO;2, 1990.

Stephens, G. L., Gabriel, P. M., and Tsay, S.-C.: Statistical radiative transport in one-dimensional media and its application to the terrestrial atmosphere, Transp. Theory Stat. Phys., 20, 139–175, https://doi.org/10.1080/00411459108203900, 1991.

Stephens, G. L., Wood, N. B., and Gabriel, P. M.: An assessment of the parameterization of subgrid-scale cloud effects on radiative transfer. Part I: Vertical overlap, J. Atmos. Sci., 61, 715 – 732, https://doi.org/10.1175/1520-0469(2004)061<0715:AAOTPO>2.0.CO;2, 2004.

Stevens, B. and Bony, S.: What are climate models missing?, Science, 340, 1053–1054, https://doi.org/10.1126/science.1237554, 2013.

Takano, Y. and Liou, K.-N.: Solar radiative transfer in cirrus clouds. Part I: Single-scattering and optical properties of hexagonal ice crystals, J. Atmos. Sci., 46, 3 – 19, https://doi.org/10.1175/1520-0469(1989)046<0003:SRTICC>2.0.CO;2, 1989.

Unterstrasser, S. and Stephan, A.: Far field wake vortex evolution of two aircraft formation flight and implications on young contrails, The Aeronaut. J., 124, 667–702, https://doi.org/10.1017/aer.2020.3, 2020.

van de Hulst, H. C.: Light scattering by small particles, Courier Corporation, 1981.

Wendisch, M., Yang, P., and Pilewskie, P.: Effects of ice crystal habit on thermal infrared radiative properties and forcing of cirrus, J. Geophys. Res. Atmos., 112, D08 201, https://doi.org/10.1029/2006JD007899, 2007.

Wilber, A. C.: Surface emissivity maps for use in satellite retrievals of longwave radiation, NASA, https://ntrs.nasa.gov/citations/19990100634, last access: 16 January 2023, 1999.

Wolf, K., Bellouin, N., and Boucher, O.: Simulated top-of-atmosphere (15 km) downward and upward solar and thermal-infrared irradiances and ice cloud optical thickness; calculated solar, TIR and net cloud radiative effect. Simulated with ice crystal properties for aggregates, droxtals, and plates based on Yang (2000)., https://doi.org/10.5281/zenodo.7593464, 2023.

Wylie, D. P. and Menzel, W. P.: Eight years of high cloud statistics using HIRS, J. Climate, 12, 170 – 184, https://doi.org/10.1175/1520-0442(1999)012<0170:EYOHCS>2.0.CO;2, 1999.

Yang, P., Liou, K. N., Wyser, K., and Mitchell, D.: Parameterization of the scattering and absorption properties of individual ice crystals, J. Geophys. Res. Atmos., 105, 4699–4718, https://doi.org/10.1029/1999JD900755, 2000.

Yang, P., Baum, B. A., Heymsfield, A. J., Hu, Y. X., Huang, H.-L., Tsay, S.-C., and Ackerman, S.: Single-scattering properties of droxtals, J. Quant. Spectrosc. Radiat. Transfer, 79-80, 1159–1169, https://doi.org/10.1016/S0022-4073(02)00347-3, 2003.

Yang, P., Wei, H., Huang, H.-L., Baum, B. A., Hu, Y. X., Kattawar, G. W., Mishchenko, M. I., and Fu, Q.: Scattering and absorption property database for nonspherical ice particles in the near- through far-infrared spectral region, Appl. Opt., 44, 5512–5523, https://doi.org/10.1364/AO.44.005512, 2005.

Yang, P., Hong, G., Dessler, A. E., Ou, S. S. C., Liou, K.-N., Minnis, P., and Harshvardhan: Contrails and Induced Cirrus: Optics and Radiation, Bull. Am. Meteorol. Soc., 91, 473 – 478, https://doi.org/10.1175/2009BAMS2837.1, 2010.

Yang, P., Bi, L., Baum, B. A., Liou, K.-N., Kattawar, G. W., Mishchenko, M. I., and Cole, B.: Spectrally consistent scattering, absorption, and polarization properties of atmospheric ice crystals at wavelengths from 0.2 to 100 μm, J. Atmos. Sci., 70, 330 – 347, https://doi.org/10.1175/JAS-D-12-039.1, 2013.

Zhang, Y., Laube, M., and Raschke, E.: Numerical simulations of cirrus properties, Contributions to Atmospheric Physics, 67, 109–120, 1994.

Zhang, Y., Macke, A., and Albers, F.: Effect of crystal size spectrum and crystal shape on stratiform cirrus radiative forcing, Atmos. Res., 52, 59–75, https://doi.org/10.1016/S0169-8095(99)00026-5, 1999.